Methylamine and other simple N-bearing species in the hot cores NGC 6334I MM1-3

Bøgelund, E.G.; McGuire, B.A.; Hogerheijde, M.R.; van Dishoeck, E.F.; Ligterink, N.F.W.

[Link to publication](#)

Methylamine and other simple N-bearing species in the hot cores NGC 6334I MM1–3

Eva G. Bøgelund[1], Brett A. McGuire[2], Michiel R. Hogerheijde[1,3],
Ewine F. van Dishoeck[1,4], and Niels F. W. Ligterink[1,5]

[1] Leiden Observatory, Leiden University, PO Box 9513, 2300 RA Leiden, The Netherlands
 e-mail: `bogelund@strw.leidenuniv.nl`
[2] National Radio Astronomy Observatory, 520 Edgemont Rd, Charlottesville, VA 22903, USA
[3] Anton Pannekoek Institute for Astronomy, University of Amsterdam, Science Park 904, 1098 XH Amsterdam, The Netherlands
[4] Max-Planck Institut für Extraterrestrische Physik, Giessenbachstr. 1, 85748 Garching, Germany
[5] Center for Space and Habitability (CSH), University of Bern, Sidlerstrasse 5, 3012 Bern, Switzerland

ABSTRACT

Context. In the search for the building blocks of life, nitrogen-bearing molecules are of particular interest since nitrogen-containing bonds are essential for the linking of amino acids and ultimately the formation of larger biological structures. The elusive molecule methylamine (CH_3NH_2) is thought to be a key pre-biotic species but has so far only been securely detected in the giant molecular cloud Sagittarius B2.

Aims. We identify CH_3NH_2 and other simple nitrogen-bearing species involved in the synthesis of biologically relevant molecules towards three hot cores associated with the high-mass star-forming region NGC 6334I, located at a distance of 1.3 kpc. Column density ratios are derived in order to investigate the relevance of the individual species as precursors of biotic molecules.

Methods. High sensitivity, high angular and spectral resolution observations obtained with the Atacama Large Millimeter/submillimeter Array were used to study transitions of CH_3NH_2, CH_2NH, NH_2CHO, and the ^{13}C- and ^{15}N-methyl cyanide (CH_3CN) isotopologues, detected towards NGC 6334I. Column densities are derived for each species assuming local thermodynamic equilibrium and excitation temperatures in the range 220–340 K for CH_3NH_2, 70–110 K for the CH_3CN isotopologues and 120–215 K for NH_2CHO and CH_2NH.

Results. We report the first detections of CH_3NH_2 towards NGC 6334I with column density ratios with respect to CH_3OH of 5.9×10^{-3}, 1.5×10^{-3} and 5.4×10^{-4} for the three hot cores MM1, MM2, and MM3, respectively. These values are slightly lower than the values derived for Sagittarius B2 but higher by more than an order of magnitude as compared with the values derived for the low-mass protostar IRAS 16293–2422B. The column density ratios of NH_2CHO, $^{13}CH_3CN$, and $CH_3C^{15}N$ with respect to CH_3OH are $(1.5 - 1.9) \times 10^{-4}$, $(1.0 - 4.6) \times 10^{-3}$ and $(1.7 - 3.0) \times 10^{-3}$ respectively. Lower limits of 5.2, 1.2, and 3.0 are reported for the CH_3NH_2 to CH_2NH column density ratio for MM1, MM2, and MM3 respectively. These limits are largely consistent with the values derived for Sagittarius B2 and higher than those for IRAS 16293–2422B.

Conclusions. The detections of CH_3NH_2 in the hot cores of NGC 6334I hint that CH_3NH_2 is generally common in the interstellar medium, albeit that high-sensitivity observations are essential for the detection of the species. The good agreement between model predictions of CH_3NH_2 ratios and the observations towards NGC 6334I indicate a main formation pathway via radical recombination on grain surfaces. This process may be stimulated further by high grain temperatures allowing a lager degree of radical mobility. Further observations with ALMA will help evaluate the degree to which CH_3NH_2 chemistry depends on the temperature of the grains in high- and low-mass star-forming regions respectively.

Key words. astrochemistry – methods: observational – stars: protostars – ISM: individual objects: NGC 6334I – submillimeter: ISM

1. Introduction

A number of molecular species that are recognised as precursors to biologically relevant molecules have in recent years been identified in the interstellar medium (ISM). These so-called pre-biotic species (see Herbst & van Dishoeck 2009, and references therein) are involved in the formation of, for example, amino acids, the main constituents of proteins, and nucleobases, the fundamental components of DNA and RNA, and thereby constitute the basis for the building blocks of life.

Among the pre-biotic molecules are the species methylamine (CH_3NH_2) and methanimine (CH_2NH), the simplest primary amine- (–NH_2) and imine- (–$C = N$–) containing species,

respectively. Experiments in which interstellar ice analogues are subjected to thermal processing or irradiation by UV photons have shown that both CH_3NH_2 and CH_2NH are involved in reactions that form amino acids, and have specifically been proven to engage in the synthesis of glycine (NH_2CH_2COOH), the smallest member of the amino acid family (Holtom et al. 2005; Lee et al. 2009; Bossa et al. 2009; Danger et al. 2011). The formation of glycine within or upon the icy mantles of interstellar dust grains is consistent with theoretical models by Garrod (2013) who trace and couple the gas-phase, grain-surface and bulk ice chemistry during the formation of hot cores. In addition, the connection between CH_3NH_2 and glycine has been established through the proposed formation of both these species from a common

set of precursors present in carbonaceous chondrite meteorites (Aponte et al. 2017) including carbon monoxide (CO), ammonia (NH_3), hydrogen cyanide (HCN), and carbon dioxide (CO_2).

Another example of a simple progenitor of biotic molecules is formamide (NH_2CHO), the simplest amide (–NH–(C = O)–), which has the same chemical structure as the peptide bonds that link amino acids and thereby form the backbone of larger protein structures. NH_2CHO has also been shown to be involved in the formation of nucleobases and nucleobase analogues in processes which use minerals and metal oxides, including samples of primitive meteoroids, as catalysts (Saladino et al. 2006, 2016; Kumar et al. 2014).

Lastly, due to its cyanide (–CN) group, the molecule methyl cyanide (acetonitrile, CH_3CN) is also of interest in relation to the synthesis of pre-biotic molecules. This is due to the importance of C–N bonds for the formation of peptide structures. Reactions involving cyanides, especially HCN and its derivatives, are therefore regarded as the foundation of the formation of complex structures such as proteins, lipids and nuclei acids (Matthews & Minard 2006; Patel et al. 2015). In addition, Goldman et al. (2010) propose that shock-induced C–N bonds due to cometary impacts on the early Earth provide a potential synthesis route for amino acids which is independent of the pre-existing atmospheric conditions and materials on the planet. In summary, continued observations and searches for CH_3NH_2, CH_2NH, NH_2CHO, CH_3CN, and other pre-biotic species in the ISM, as well as in solar system bodies, are of high interest in order to establish the relevance of the respective species in connection to the emergence of life on Earth, and potentially on other (exo)planets and moons.

NH_2CHO and CH_3CN are routinely detected towards high- and low-mass hot cores (Cazaux et al. 2003; Bisschop et al. 2007; Kahane et al. 2013), and have in addition been identified towards a number of comets (see review by Mumma & Charnley 2011), in particular the bright comet Hale–Bopp (e.g. Bockelée-Morvan et al. 1997; Remijan et al. 2008) and comet 67P/Churyumov-Gerasimenko (hereafter 67P), the target of ESA's Rosetta mission (Goesmann et al. 2015; Altwegg et al. 2017). In addition, CH_3CN was the first complex organic molecule (COM) to also be detected in a protoplanetary disk (Öberg et al. 2015) and thereby became one of the few pre-biotic species whose presence could be traced throughout all formation phases from the earliest stages of star formation to the last remnants in comets.

Despite the lack of firm detections of CH_2NH in comets (Irvine et al. 1998; Crovisier et al. 2004), this species has also been detected towards a variety of interstellar sources including giant molecular clouds (Dickens et al. 1997) and high- and low-mass protostellar systems (Suzuki et al. 2016; Ligterink et al. 2018). In contrast to these detections, the structurally similar species CH_3NH_2 has proven to be an especially elusive molecule and for a long time was only securely detected towards the high-mass source Sagittarius B2 (hereafter Sgr B2) located in the Galactic centre (e.g. Kaifu et al. 1974; Belloche et al. 2013). Recently, the molecule was also detected towards the hot core G10.47 + 0.03 by Ohishi et al. (2017) who also report a tentative detection towards NGC 6334I although the low signal-to-noise and variations in v_{LSR} between transitions of the species makes the detection unclear. A tentative detection was also reported towards Orion KL by Pagani et al. (2017). In addition, a series of non-detections have been reported towards a number of high-mass young stellar objects (YSOs, Ligterink et al. 2015) and a very stringent upper limit has been set on the abundance of the species in the low-mass Sun-like protostar IRAS 16293–2422B (Ligterink et al. 2018). Recently, the species has also

been detected in the coma of comet 67P (Altwegg et al. 2017). These detections (and upper limits) indicate a range of CH_3NH_2 abundances with respect to CH_3OH, with that of IRAS 16293–2422B being at least one to two orders of magnitude lower than the values derived for Sgr B2. The discrepancies between the detections in Sgr B2 and the non-detections elsewhere has led to the suggestion that formation pathways for CH_3NH_2 are not very efficient and that they may depend strongly on the conditions which characterise the individual regions. Based on the detections of CH_3NH_2 in Sgr B2 it has therefore been speculated that the presence of relatively high dust grain temperatures or strong radiation fields enhance CH_3NH_2 formation.

The formation of CH_3NH_2 is discussed in a number of studies. On interstellar dust grains, two main formation pathways have been proposed: the first is a hydrogenation sequence starting from hydrogen cyanide: $HCN + 2H \rightarrow CH_2NH + 2H \rightarrow CH_3NH_2$ (Theule et al. 2011). Although the efficiency of formation via this pathway is ill constrained, the same hydrogenation mechanism has been used in glycine formation models to form the intermediate CH_2NH_2 radical (Woon 2002). The second formation route involves radical recombination reactions between a methyl (–CH_3) and an amino group: $CH_3 + NH_2 \rightarrow CH_3NH_2$. This pathway has been included in the astrochemical models presented by Garrod et al. (2008) as the main formation route for CH_3NH_2. Experimentally, electron and photon irradiated interstellar ice analogues, consisting of CH_4 and NH_3, have been shown to result in formation of CH_3NH_2 (Kim & Kaiser 2011; Förstel et al. 2017). Although in dark clouds, both CH_3 and NH_2 can also result from H-addition to atomic C and N and therefore photodissociation is not critical for the formation of the radicals. In the gas-phase, the radical-neutral reaction $CH_3 + NH_3 \rightarrow CH_3NH_2 + H$ has been proposed to be the main CH_3NH_2 formation route. This is based on the observational study of Sgr B2 conducted by Halfen et al. (2013) who also argue that the formation of CH_3NH_2 through successive hydrogenation of CH_2NH is unlikely due to the large difference in rotational temperature, 44 ± 13 K in the case of CH_2NH and 159 ± 30 K in the case of CH_3NH_2, derived through rotational temperature diagrams. This difference makes it unlikely that the molecules occupy the same regions thereby making CH_2NH an unlikely synthetic precursor of CH_3NH_2. A dominant gas-phase formation route for CH_2NH is also reported by Suzuki et al. (2016) although they note that hydrogenation of solid-phase CH_2NH can also form CH_3NH_2. Additional detections of CH_3NH_2 and related species, preferably towards a large number of different sources, will therefore provide valuable information and help distinguish between formation routes and conditions required for the formation of this species.

In this work, CH_3NH_2 along with other simple pre-biotic nitrogen-bearing species, in particular CH_2NH, CH_3CN, and NH_2CHO, are studied towards three dense cores within the giant molecular cloud complex NGC 6334. The NGC 6334 region, located in the constellation Scorpius in the southern hemisphere, is a very active high-mass star-forming region composed of six sub-regions denoted I – V and I(N) (see review by Persi & Tapia 2008, and references therein). Water and methanol (CH_3OH) maser studies have placed the region at a mean distance of 1.3 kpc from the Sun (Chibueze et al. 2014; Reid et al. 2014), equivalent to a galactocentric distance (d_{GC}) of ~7.02 kpc. The focus of this work is on the deeply embedded source NGC 6334I which is located in the north-eastern part of the cloud. The morphology of this source has been studied in detail by Brogan et al. (2016) who identify a number of distinct peaks in the sub-millimetre continuum and assign these to individual

high-mass star-forming systems. The region has a very rich molecular inventory as demonstrated by Zernickel et al. (2012) who identify a total of 46 molecular species towards NGC 6334I including CH_2NH, CH_3CN, and NH_2CHO but not CH_3NH_2.

This paper presents the first detection of CH_3NH_2 towards NGC 6334I. The work is based on high sensitivity, high spectral and angular resolution data obtained with the Atacama Large Millimeter/submillimeter Array (ALMA). Previous searches for CH_3NH_2 have, for the most part, been carried out with single dish telescopes, which are generally less sensitive when compared with interferometric observations, and have therefore focused mainly on the bright hot cores associated with the Galactic central region. With the unique sensitivity and resolving power of ALMA this is changing and the weak lines associated with CH_3NH_2 can now be probed in regions away from the Galactic centre, such as NGC 6334I, as well as in low-mass systems (Ligterink et al. 2018).

The paper is structured in the following way: in Sect. 2 the observations and analysis methodology are introduced. Section 3 presents the observed transitions of each of the studied species and the model parameters used to reproduce the data. In Sect. 4 the derived column density ratios are discussed and compared between the regions in NGC 6334I as well as to the values derived for other high- and low-mass objects. Finally, our findings are summarised in Sect. 5.

2. Observations and method

2.1. Observations

Observations of NGC 6334I were carried out with ALMA in Cycle 3 on January 17, 2016 using the ALMA Band 7 receivers (covering the frequency range 275 – 373 GHz). Three spectral windows centred around 301.2, 302.0, and 303.7 GHz covering a total bandwidth of ~3 GHz were obtained. The observations have spectral and angular resolutions of 1 km s^{-1} and ~1″ (equivalent to ~1300 au at the distance of NGC 6334I) respectively. The data were interactively self-calibrated and continuum subtracted using the most line-free channels. A detailed description of this reduction procedure may be found in Brogan et al. (2016) and Hunter et al. (2017) while a summary of all observing parameters are listed in Table 1 of McGuire et al. (2017). After calibration the data were corrected for primary beam attenuation.

2.2. Method

For the analysis of CH_3NH_2 and related species three spectra, extracted at different locations across the NGC 6334I region, are used. For consistency we use the same locations and naming as in Bøgelund et al. (2018) and focus on the regions MM1 II, MM2 I, and MM3 I. These regions are associated with each of the continuum sources MM1, MM2, and MM3 making it possible to compare the abundances of the various species across the three hot cores. Due to the greater lines widths characterising the central part of the MM1 region and the bright continuum emission, which in some cases result in negative features after continuum subtraction has been applied, we select a region away from the main continuum peak where weak emission line features are more easily identified. The extracted spectra are the average of a 1″00 × 0″74 region, equivalent to the area of the synthesised beam. The coordinates of the central pixel of each of the regions are (J2000 17^{h}20^{m}53.371^s, −35°46′57″013), (J2000 17^{h}20^{m}53.165^s, −35°46′59.231″) and (J2000 17^{h}20^{m}53.417^s, −35°47′00″697) for MM1 II, MM2 I, and MM3 I respectively. For each of the extracted spectra, the

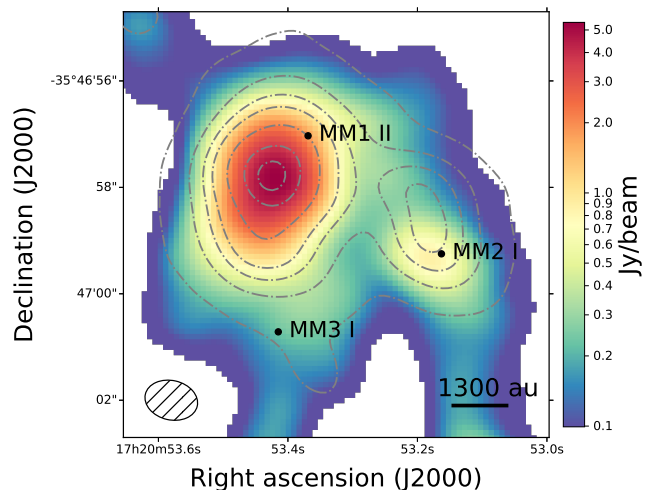**Fig. 1.** 1 mm continuum image of the NGC 6334I region with the velocity integrated intensity map of the $^{13}CH_3CN$ transition at 303.610 GHz overlaid in grey contours (levels are [3, 20, 40, 60, 100, 150, 180]σ with $\sigma = 0.07$ Jy beam^{-1} km s^{-1}). Pixels with values less than 1% of the peak intensity have been masked out. The locations at which spectra have been extracted are marked for each region. The synthesised beam (~1300 × 962 au) is shown in the bottom left corner.

rms noise is calculated after careful identification of line-free channels. These are ~0.9 K (68 mJy beam^{-1}) for MM1, ~0.6 K (45 mJy beam^{-1}) for MM2, and ~0.04 K (3 mJy beam^{-1}) for MM3. The difference in the estimated rms noise values reflects the large variations in brightness and line density over the three regions. An overview of the NGC 6334 I region and the locations at which spectra have been extracted is shown in Fig. 1.

In order to identify transitions of CH_3NH_2, CH_2NH, CH_3CN, and NH_2CHO, as well as to constrain the column density and excitation temperature of the species at each of the studied positions, synthetic spectra are produced using the CASSIS[1] line analysis software. The spectroscopic data for CH_2NH and the methyl cyanide and formamide isotopologues are adopted from the JPL[2] and CDMS[3] molecular databases (CH_2NH: Kirchhoff et al. 1973; $^{13}CH_3CN$ and $CH_3C^{15}N$: Müller et al. 2009 and references therein; NH_2CHO and $NH_2^{13}CHO$: Kukolich & Nelson 1971; Gardner et al. 1980; Blanco et al. 2006; Motiyenko et al. 2012 and references therein). For CH_3NH_2, the spectroscopic data are taken from Motiyenko et al. (2014). Assuming local thermodynamic equilibrium (LTE) and optically thin lines, synthetic spectra are constructed for each species. This is done by providing CASSIS with a list of parameters including excitation temperature, T_{ex} (K), column density of the species, N_s (cm^{-2}), source velocity, v_{LSR} (km s^{-1}), line width at FWHM (km s^{-1}), and angular size of the emitting region, θ_s (″), assumed to be equal to the size of the synthesised beam.

Excitation temperatures and column densities are determined for the detected species by creating grids of model spectra varying T_{ex} and N_s and identifying the model spectrum with the minimal χ^2 as the best fit. The CASSIS software computes the χ^2 value for each of the model spectra taking into account the rms noise of the observed spectrum and the calibration uncertainty
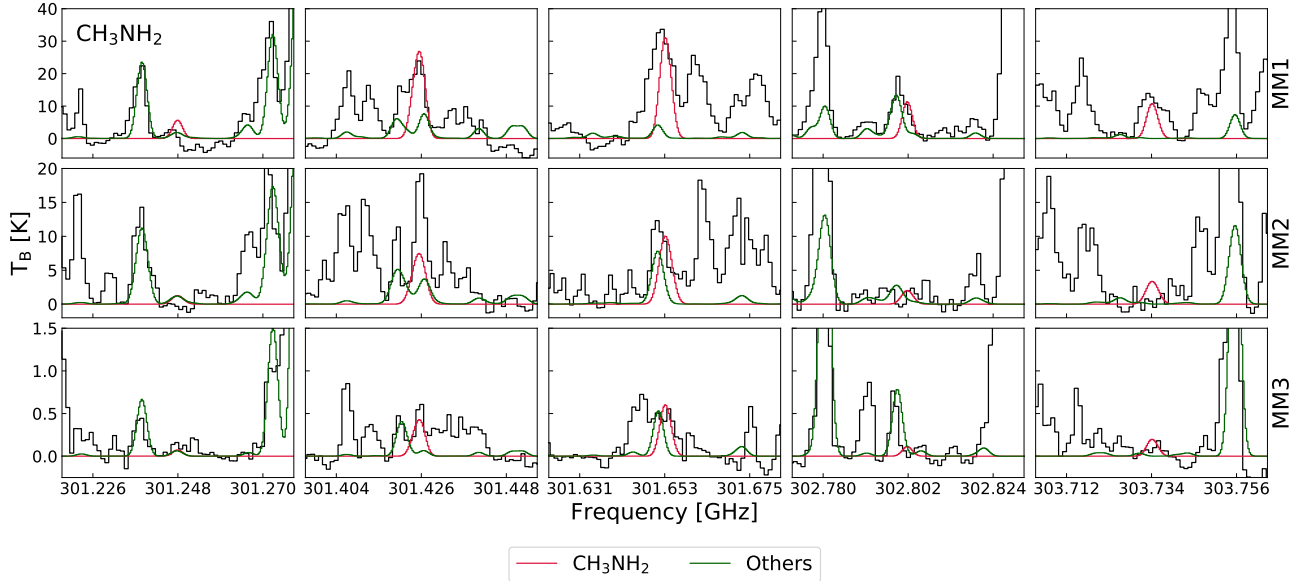

Fig. 2. CH$_3$NH$_2$ transitions detected towards NGC 6334I. Red and green lines represent the synthetic spectrum of CH$_3$NH$_2$ and the sum of spectra of other contributing species respectively. The abscissa is the rest frequency with respect to the radial velocity towards each of the hot cores (listed in Table 2). The data are shown in black. *Top panels*: MM1 II. *Middle panels*: MM2 I. *Bottom panels*: MM3 I.

(assumed to be ~10%). χ^2 is defied as:

$$\chi^2 = \sum_{i=1}^{N} \left(\frac{(I_{\mathrm{obs},i} - I_{\mathrm{model},i})}{\sigma_i} \right)^2, \qquad (1)$$

where $I_{\mathrm{obs},i}$ and $I_{\mathrm{model},i}$ is the intensity of the observed and modelled spectrum in channel i, respectively, $\sigma_i = \sqrt{\mathrm{rms}^2 + (0.1 \times I_{\mathrm{obs},i})^2}$ and N is the number of fitted points, that is, the number of channels covered by each of the transitions to which the model is optimised (we consider the channels within a range of $\pm 2 \times FWHM$). Table A.1 lists the model grids for each of the fitted species. Since only a single CH$_2$NH transition and just two NH$_2$CHO transitions are detected, the excitation temperatures of these species cannot be constrained from the data. The reported CH$_2$NH and NH$_2$CHO column densities are therefore derived assuming T_{ex} to be fixed at the value derived for CH$_3$OH in each region by Bøgelund et al. (2018). These are 215 K for region MM1 II, 165 K for region MM2 I, and 120 K for region MM3 I. The uncertainty on N_{s} and T_{ex} is listed as the standard deviation of model spectra with χ^2 within 1σ of the best-fit model. For N_{s}, the highest uncertainty is approximately 30% while the uncertainty on T_{ex} is up to 65%. Through the propagation of errors, the uncertainty on listed column density ratios is conservatively estimated to be ~40% ($\sqrt{2} \times 30\%$). Because the velocity structure of NGC 6334I is not well-known, the source velocity and FWHM line widths characterising each region are fixed throughout the fitting procedure so as not to introduce additional free parameters. As is clear from Fig. 2 and Figs. D.1–D.3, the fixed v_{LSR} and line widths are consistent with the data for all species. However, examples of molecules detected towards the same region but characterised by different physical parameters have been reported (see e.g. Halfen et al. 2013).

For each identified CH$_3$NH$_2$, CH$_2$NH, CH$_3$CN, and NH$_2$CHO transition, a thorough search for potential blending species is conducted. This search is carried out carefully in the following steps: (1) All catalogued species, that is to say all species which are listed in the JPL or CDMS databases and which have transitions at frequencies that overlap with those of

CH$_3$NH$_2$, CH$_2$NH, CH$_3$CN, or NH$_2$CHO, are identified. (2) For each potential blending species a synthetic spectrum is produced and optimised so that the column density of that species is maximised. This is done while ensuring that none of the other transitions belonging to the same species, and which are covered by the data, are overproduced with respect to the data. (3) If the potential blending species are isotopologues, step 2 is repeated for the parent species in order to ensure that column densities are consistent between isotopologues of the same species. (4) Once the spectra of the individual potential blending species have been optimised, they are summed to obtain a full spectrum for each of the three regions. Two fits are then preformed; the first fit takes only the studied species into account and is used to set an upper limit on the column density for each of these; the second fit includes the contributions from all potential blending species.

By including the maximised contribution from the potential blending species to the modelled spectrum, the contributions from CH$_3$NH$_2$, CH$_2$NH, CH$_3$CN, and NH$_2$CHO to the same modelled spectrum are minimised and consequently the most stringent limits on the column densities of these species are achieved. It should be noted however, that maximising the column densities of some potential blending species, in particular deuterated isotopologues, leads to values which are unrealistically high when compared with parent species and therefore should be seen purely as a method to conservatively constrain the amounts of CH$_3$NH$_2$, CH$_2$NH, CH$_3$CN, and NH$_2$CHO. The full list of potential blending species as well as model parameters are listed in Table E.1. Finally, a ^{12}C/^{13}C ratio of 62, a ^{16}O/^{18}O ratio of 450, and a ^{14}N/^{15}N ratio of 422 is adopted throughout the paper, all derived assuming $d_{\mathrm{GC}} = 7.02$ kpc and the relations for ^{12}C/^{13}C, ^{16}O/^{18}O, and ^{14}N/^{15}N reported by Milam et al. (2005) and Wilson (1999).

3. Results

In the following sections the detections of CH$_3$NH$_2$ will be discussed in detail alongside a summary of the main results regarding the detections of CH$_2$NH, CH$_3$CN, and NH$_2$CHO (see Appendix D for full discussion of these species). Transition

Table 1. Summary of lines.

Transition		Catalogue frequency	E_{up}	A_{ij}	Catalogue
$(QN)_{up}$ [a]	$(QN)_{low}$ [a]	(MHz)	(K)	$\times 10^{-5}$ (s^{-1})	
		CH_2NH			
$15_{2,13}$ 14	$14_{3,12}$ 13	302 565.4318	408.72	6.61	JPL
$15_{2,13}$ 16	$14_{3,12}$ 15	302 565.4883	408.72	6.64	
$15_{2,13}$ 15	$14_{3,12}$ 14	302 566.3219	408.72	6.61	
		CH_3NH_2 [b]			
16 2 A2 15	15 3 A1 14	301 247.6939	305.21	1.37	Motiyenko et al. (2014)
16 2 A2 17	15 3 A1 16	301 247.7074	305.21	1.55	
16 2 A2 16	15 3 A1 16	301 247.9700	305.21	1.46	
13 2 B2 13	13 1 B1 13	301 424.0139	210.13	2.69	
13 2 B2 14	13 1 B1 14	301 425.6883	210.13	2.90	
13 2 B2 13	13 1 B1 12	301 425.8175	210.13	2.50	
9 0 B2 8	8 1 B1 7	301 653.3284	95.93	2.68	
9 0 B2 10	8 1 B1 9	301 653.4789	95.93	3.36	
9 0 B2 9	8 1 B1 8	301 654.7988	95.93	3.00	
16 7 B1 16	17 6 B2 17	302 801.6275	480.13	0.83	
16 7 B2 16	17 6 B1 17	302 801.6306	480.15	0.83	
16 7 B1 17	17 6 B2 18	302 801.7834	480.13	0.88	
16 7 B2 17	17 6 B1 18	302 801.7866	480.13	0.88	
16 7 B1 15	17 6 B2 16	302 801.7912	480.13	0.78	
16 7 B2 15	17 6 B1 16	302 801.7943	480.13	0.78	
9 0 E2+1 8	8 1 E2+1 7	303 733.9183	96.20	2.63	
9 0 E2+1 10	8 1 E2+1 9	303 734.0611	96.20	3.29	
9 0 E2+1 9	8 1 E2+1 8	303 735.3214	96.20	2.94	
		$^{13}CH_3CN$			
17_5	16_5	303 518.8535	310.00	222	CDMS
17_4	16_4	303 570.0991	245.64	230	
17_3	16_3	303 609.9710	195.57	236	
17_2	16_2	303 638.4820	159.80	240	
17_1	16_1	303 655.5770	138.33	243	
17_0	16_0	303 661.2780	131.18	243	
		$CH_3C^{15}N$			
17_4	16_4	303 187.8887	245.49	229	
17_3	16_3	303 227.9360	195.41	235	
17_2	16_2	303 256.5540	159.64	240	
17_1	16_1	303 273.7300	138.17	242	
17_0	16_0	303 279.4560	131.01	243	
		NH_2CHO			
$15_{1,15}$	$14_{1,14}$	303 450.2040	120.01	205	CDMS
$14_{1,13}$	$13_{1,12}$	303 660.5390	113.01	204	
		$NH_2^{13}CHO$			
$15_{1,15}$	$14_{1,14}$	302 553.9861	119.61	203	CDMS
$14_{1,13}$	$13_{1,12}$	303 111.8280	112.78	203	

Notes. [a]Quantum numbers for CH_2NH are J_{K_a,K_c} F. Quantum numbers for CH_3NH_2 are J K_a Γ F, following the notation of Motiyenko et al. (2014). Quantum numbers for $^{13}CH_3CN$ and $CH_3C^{15}N$ are J_K. Quantum numbers for NH_2CHO and $NH_2^{13}CHO$ are J_{K_a,K_c}. [b]Only lines with $A_{ij} > 10^{-6} s^{-1}$ are listed.

frequencies and line data for all species are listed in Table 1, while integrated line intensities of a select number of lines in the observational data are listed in Table B.1. In the case of CH_3NH_2, detected lines have E_{up} values ranging from 96 to 480 K. For each of the studied regions and species the column density and excitation temperature of the best-fit synthetic spectrum are derived. In Sect. 4 these values and their ratios with respect to CH_3OH and CH_3NH_2 will be compared between the individual regions of NGC 6334I but also discussed in relation to those derived for other objects. The parameters of the best-fit models are listed in Table 2 and all transitions and modelled

spectra of CH_3NH_2 and other species are plotted in Fig. 2 and Figs. D.1–D.3 respectively.

3.1. Methylamine CH_3NH_2

For CH_3NH_2, five transitional features (all covering multiple hyperfine components) are identified towards NGC 6334I. These are plotted in Fig. 2. The CH_3NH_2 transitions are not isolated lines but blended with transitions of other species. Nevertheless, and despite the contributions from the potential blending molecules, it is evident that the data cannot be reproduced

Table 2. Best-fit model parameters.

	MM1 II		MM2 I		MM3 I	
$v_{\rm LSR}$ (km s^{-1})	[−6.7]		[−9.0]		[−9.0]	
$FWHM$ (km s^{-1})	[3]		[3.5]		[3]	
$\theta_{\rm s}$ ($''$)	[1]		[1]		[1]	
	$T_{\rm ex}$ (K)	$N_{\rm s}$ (cm^{-2})	$T_{\rm ex}$ (K)	$N_{\rm s}$ (cm^{-2})	$T_{\rm ex}$ (K)	$N_{\rm s}$ (cm^{-2})
CH_2NH	[215]	$\leq 5.2 \times 10^{16}$	[165]	$\leq 5.0 \times 10^{16}$	[120]	$\leq 10^{15}$
CH_3NH_2	340 ± 60	$(2.7 \pm 0.4) \times 10^{17}$	230 ± 30	$(6.2 \pm 0.9) \times 10^{16}$	220 ± 30	$(3.0 \pm 0.6) \times 10^{15}$
$^{13}CH_3CN$	70 ± 10	$(3.4 \pm 1.0) \times 10^{15}$	80 ± 25	$(1.4 \pm 0.5) \times 10^{15}$	90 ± 15	$(9.0 \pm 0.8) \times 10^{13}$
$CH_3C^{15}N$	110 ± 50	$(3.3 \pm 0.5) \times 10^{14}$	[80]	$(1.8 \pm 0.4) \times 10^{14}$	70 ± 45	$(2.3 \pm 0.7) \times 10^{13}$
NH_2CHO	[215]	$(7.0 \pm 1.7) \times 10^{15}$	[165]	$(7.6 \pm 0.8) \times 10^{15}$	[120]	$\leq 5.0 \times 10^{13}$
$NH_2^{13}CHO^a$	[215]	$\leq 2.0 \times 10^{15}$	[165]	$\leq 5.0 \times 10^{14}$	−	−

Notes. Values in square brackets are fixed. Excitation temperatures for CH_3NH_2 and CH_3CN are the values of the best-fit respective models while $T_{\rm ex}$ for CH_2NH and NH_2CHO is fixed at the best-fit model value derived for CH_3OH (Bøgelund et al. 2018). In the MM2 region, the excitation temperature for $CH_3C^{15}N$ is not well constrained and is therefore adopted from $^{13}CH_3CN$. Listed uncertainties are the standard deviation of models with χ^2 within 1σ of the best-fit model.

without including CH_3NH_2 in the model, especially for the MM1 II and MM3 I regions.

MM1 II. For MM1 II the CH_3NH_2 transitions are well reproduced by a model with a column density of 2.7×10^{17} cm^{-2} and an excitation temperature of 340 K. The uncertainty on each of these values is less than 20%. For lower excitation temperatures, down to 100 K, the column density is consistent with that derived for 340 K within a factor of approximately two. The same is true for $T_{\rm ex}$ up to 500 K although for very low temperatures, down to 50 K, the column density can no longer be well-constrained. Also, since the variation between the column density of the fit which only takes into account CH_3NH_2 and the fit which includes all potential blending species is less then 30%, we consider it very probable that the features in the spectrum of this region are due to CH_3NH_2. The fact that the features cannot be reproduced without including CH_3NH_2 in the model makes the detection even more convincing. Around the transition located at 301.248 GHz, a slight negative offset in the baseline is seen. This is likely caused by continuum over-subtraction resulting in a negatively displaced baseline which makes the model transition at this location appear brighter than the observed one.

MM2 I. The best-fit model for region MM2 I has a column density equal to 6.2×10^{16} cm^{-2} and an excitation temperature of 230 K. This model is optimised to fit all of the covered CH_3NH_2 transitions, although only two of these, located at 301.426 and 301.653 GHz, are considered fully detected. The remaining transitions, located at 301.248, 302.802, and 303.734 GHz, are considered tentative detections. This is because these transitions are blended with emission from other species (lines at 301.248 and 302.802 GHz) or because no clear line is visible in the observed spectrum at the expected location (line at 303.734 GHz). The tentative detections are included in the χ^2 minimisation, as they help constrain the best-fit model. For MM2, the uncertainty on $N_{\rm s}$ and $T_{\rm ex}$ is ~15%. Varying the excitation temperature down to 50 and up to 500 K does not cause the value of the column density to change by more than a factor of two with respect to the best-fit value derived at 230 K. In contrast to the CH_3NH_2 features of MM1 II however, which are all well reproduced by the single-density, single-temperature model, the lines of MM2 I are not. Particularly the line ratio of the transitions at

301.426 and 301.653 GHz is off and cannot be reproduced by the model. Despite the fact that the upper state energy of the transitions is fairly different, ~210 K for the 301.426 GHz transitions and ~96 K for the 301.653 GHz transitions, introducing a two-component model to account for a warm and cool emission region respectively, does not improve the fit. While the transition at 301.653 GHz may be well reproduced by a model with an excitation temperature of ~50 K, addition of any higher excitation temperature-components to the model results in modelled line intensities that vastly overshoot the transition at 301.653 GHz with respect to the data while the intensity of the lines at 301.426 GHz remains much weaker than the observed line. The behaviour of this last transition is especially puzzling since none of the species included in either the JPL or CDMS catalogues are able to reproduce the observed data feature. One possible explanation is of course that the feature in the spectrum of MM2 I is due to transitions of some unknown species (or unknown transition of a known species) which is not included in the spectroscopic databases. However, if that is the case, this unknown species is particular to the MM2 I region and does not significantly affect regions MM1 II and MM3 I where the respective CH_3NH_2 models correspond well with the observations.

The dissimilarity between the CH_3NH_2 model spectrum and the observations could also indicate that the critical density for individual transitions in the MM2 I region may not be reached, removing the region from LTE. Thus, a scenario in which the density of region MM2 is so low that the critical density of one transition is reached, while that of another transition is not, could explain why the model predictions are not able to reproduce the CH_3NH_2 transitions at 301.425 and 301.655 GHz simultaneously in this region while the same lines are well-matched with the data for regions MM1 and MM3. To test this hypothesis, the collisional coefficients need to be known and the critical densities inferred for each of the transitions in question. However, since these numbers are not known for CH_3NH_2 we are unable to make the comparison but can instead conclude that it is likely that the MM2 region has a lower overall density as compared with the regions MM1 and MM3. A lower density of the MM2 region with respect to the MM1 region is consistent with the findings of Brogan et al. (2016), who estimate the dust mass associated with each of the hot cores based on their spectral

energy distribution. As in the case of MM1 II, the CH_3NH_2 features cannot be reproduced satisfactory by any other species and therefore we conclude that CH_3NH_2 is likely to be present in the region despite the inadequacy of the model to fully reproduce the data.

MM3 I. For MM3 I the best-fit column density and excitation temperature values are 3.0×10^{15} cm^{-2} and 220 K respectively. The uncertainty on these values is ~35% for T_{ex} and 20% for N_s. For fixed excitation temperatures down to 50 K and up to 500 K, the CH_3NH_2 column density remains within a factor of two of the best-fit value at 220 K. The value of the column density of the best-fit model does not change when the contributions from other species are included in the fit. As in the case of the MM1 region, the good agreement between the CH_3NH_2 model and data, especially around the transitions at 301.426 and 301.653 GHz, makes the presence of CH_3NH_2 in this region very convincing. Due to blending with other species at the location of the CH_3NH_2 transitions at 301.248 and 302.802 GHz, we consider these as tentative detections only. In the case of the transition located at 303.734 GHz, a weak line feature is present in the observed spectrum although not at the exact same location as predicted in the model spectrum. This transition is therefore also considered a tentative detection. As in the case of MM2 I, the tentative detections are included when the model spectra are optimised.

In summary, CH_3NH_2 is securely detected towards both the MM1 and MM3 regions while the detection towards MM2 is slightly less clear. The uncertainty on the CH_3NH_2 column densities is between 15 and 20%. Despite the local variations, the overall uniformity of CH_3NH_2 makes it likely that its origin is the same throughout the NGC 6334I region. In addition to the data presented here, we included in Appendix C a confirmation of the presence of CH_3NH_2 in NGC 6334I based on ALMA Band 10 observations from McGuire et al. (2018). However, due to the difference in angular resolution and extraction location, these data probe different excitation conditions and different populations of gas and therefore cannot be compared directly with the Band 7 observations discussed above. The Band 10 spectrum and modelled CH_3NH_2 transitions shown in Fig. C.1 and listed in Table C.1 are therefore included as proof of the presence of CH_3NH_2 in NGC 6334I but will not be discussed further here. A detailed analysis of the Band 10 data is presented by McGuire et al. (2018).

3.2. Summary of results on methanimine, methyl cyanide and formamide

A single (hyperfine-split) transition of CH_2NH is covered by the data and consequently no excitation temperature can be derived for this species. In addition, the transition is blended with CH_3OCHO and the column density of CH_2NH is therefore reported as an upper limit for each of the studied regions. In contrast, a total of eleven transitions belonging to the ^{13}C- and ^{15}N-methyl cyanide isotopologues are detected towards NGC 6334I. Six of these belong to $^{13}CH_3CN$ and five to $CH_3C^{15}N$. Although some transitions are blended, both isotopologues are clearly detected towards all of the studied regions. The uncertainty on the derived column densities of $^{13}CH_3CN$ and $CH_3C^{15}N$ is up to 30% while the uncertainty on the derived excitation temperatures is up to 65%. In the case of MM2, the excitation temperature for $CH_3C^{15}N$ could not be constrained and therefore the column density of this species is derived assuming T_{ex} to be the same as for $^{13}CH_3CN$. As in the case of CH_2NH, no excitation temperature can be derived for NH_2CHO

since only two of the 18 transitions of this species covered by the data are bright enough to be detected and these represent a very limited range of upper state energies, with a difference between the two of less than 10 K. In the case of the regions MM1 II and MM2 I, the features in the data at the location of the NH_2CHO transitions cannot be reproduced by any other species included in either the JPL or the CDMS catalogues. In contrast, the features detected towards the MM3 I region, may be reproduced by other species and the detection of NH_2CHO towards this region is therefore considered tentative. The uncertainty on the column density of NH_2CHO towards MM1 II and MM2 I is less than 25%. The full discussion of the detections of CH_2NH, CH_3CN, and NH_2CHO can be found in Appendix D.

4. Discussion

In this section, the column densities and excitation temperatures discussed above will be compared with the predictions of the chemical models of Garrod (2013) as well as to the values derived towards a number of other sources including the high-mass star-forming regions Sgr B2 and Orion KL, the low-mass protostar IRAS 16293–2422B, and the comet 67P. In order to do this, column density ratios for each of the studied species with respect to CH_3OH are derived, these are given in Table 3. CH_3OH is chosen as a reference because it is one of the most abundant COMs in the ISM and therefore has been studied comprehensively, also in NGC 6334I (Bøgelund et al. 2018). Secondly, in order to investigate the relation between the studied species, column density ratios of CH_3NH_2 with respect to CH_2NH, NH_2CHO, and CH_3CN are derived, these are given in Table 4. Figures 3 and 4 summarise all ratios. In the following sections the results on CH_3NH_2 and on the other species will be discussed separately.

4.1. Methylamine towards NGC 6334I

The detection of CH_3NH_2 in the hot cores of NGC 6334I presented here, combined with recent (tentative) detections by Pagani et al. (2017) towards Orion KL and Ohishi et al. (2017) towards a few high-mass objects, indicate that this molecule is more common and abundant than previously thought (see for example the upper limits on the species presented by Ligterink et al. 2015). In this case, the "lacking" CH_3NH_2-detections are more likely explained by observational biases, for example the large partition function of CH_3NH_2 resulting in relatively weaker transitions of this species as compared with, for example, NH_2CHO, rather than actual chemical variations between objects.

Within the regions of NGC 6334I, the CH_3NH_2 abundance is fairly uniform and column density ratios with respect to CH_3OH and CH_3CN show variations within factors of four and two between regions MM1 and MM2 and up to an order of magnitude between regions MM1 and MM3. The variation over the column density ratios derived using the ^{13}C- and ^{18}O-methanol iosotopologues as a reference vary with a factor of three, while the ratios derived based on the ^{13}C- and ^{15}N-methyl cyanide isotopologues vary with a factor of two. In the case of the CH_3NH_2 to NH_2CHO ratio, the variation is a factor of seven if all three regions are considered and less than a factor of five between regions MM1 II and MM2 I. This is due to the relatively low column density of NH_2CHO in MM3 I as compared with regions MM1 II and MM2 I. Similarly, the variation of the CH_3NH_2 to CH_2NH column density ratio over the three regions is within a factor of four, though the single CH_2NH line covered by the data means that these ratios should be seen as lower limits.

Table 3. Column density ratios with CH_3OH as reference.

CH3OH reference	CH3NH2/CH3OH		NH2CHO/CH3OH		CH3CN/CH3OH				References
					$^{13}CH_3CN$		$CH_3C^{15}N$		
	^{13}C	^{18}O	^{13}C	^{18}O	^{13}C	^{18}O	^{13}C	^{18}O	
MM1 II	5.9×10^{-3}	2.5×10^{-3}	1.5×10^{-4}	6.5×10^{-5}	4.6×10^{-3}	2.0×10^{-3}	3.0×10^{-3}	1.3×10^{-3}	This work
MM2 I	1.5×10^{-3}	9.2×10^{-4}	1.9×10^{-4}	1.1×10^{-4}	2.1×10^{-3}	1.3×10^{-3}	1.9×10^{-3}	1.1×10^{-3}	This work
MM3 I	5.4×10^{-4}	4.8×10^{-4}	$\leq 9.0 \times 10^{-6}$	$\leq 7.9 \times 10^{-6}$	1.0×10^{-3}	8.9×10^{-4}	1.7×10^{-3}	1.5×10^{-3}	This work
Model F	7.3×10^{-3}		0.04		4.5×10^{-4}				1
Model M	4.0×10^{-3}		0.02		2.3×10^{-4}				1
Model S	1.8×10^{-3}		0.76		3.4×10^{-4}				1
Sgr B2(M)	8.0×10^{-3}		2.5×10^{-3}		0.03				2
Sgr B2(N)	0.03		0.07		0.11				2
Sgr B2(N)	0.10		0.04		2.8×10^{-3}				3
Sgr B2(N2–5) [a]	–		$8.3 \times 10^{-3} - 0.09$ [b]		$0.06 - 0.13$				4
Orion KL Compact Ridge	–		1.7×10^{-3}		0.01				5
IRAS 16293–2422B	$\leq 5.3 \times 10^{-5}$		10^{-3}		4×10^{-3}				6, 7, 8, 9

Notes. The uncertainty on the column density ratios derived towards NGC 6334 I is estimated to be 40% (see Sect. 2). [a]Range of values derived for the cores N2, N3, N4, and N5. [b]Excluding the upper limit on NH_2CHO for N4.
References. (1) Garrod (2013); (2) Belloche et al. (2013); (3) Neill et al. (2014); (4) Bonfand et al. (2017); (5) Crockett et al. (2014); (6) Coutens et al. (2016); (7) Ligterink et al. (2018); (8) Jørgensen et al. (2018); (9) Calcutt et al. (2018).

Table 4. CH_3NH_2 column density ratios.

CH3CN reference	CH3NH2/CH2NH	CH3NH2/NH2CHO	CH3NH2/CH3CN		References
			^{13}C	^{15}N	
MM1 II	≥ 5.2	38	1.28	1.94	This work
MM2 I	≥ 1.2	8.16	0.71	0.70	This work
MM3 I	≥ 3.0	≥ 60	0.54	0.31	This work
Model F	7.27	20.5	16.3		1
Model M	1.5	24	17.1		1
Model S	0.45	2.34	5.23		1
Sgr B2(M)	31 [a]	3.21	0.25		2
Sgr B2(N)	0.75	0.44	0.31		2
Sgr B2(N)	7.14	2.08	35.7		3
Sgr B2(N)	5.49	–	–		4
Orion KL Hot Core	≤ 2.86	≤ 3.13	–		5
IRAS 16293–2422B	≤ 0.88	≤ 0.053	≤ 0.013		6, 7
Comet 67P [b]	–	≤ 0.33	≤ 2		8

Notes. The uncertainty on the column density ratios derived towards NGC 6334 I is estimated to be 40% (see Sect. 2). [a]Extended CH_2NH emission. [b]Listed as upper limits based on the discussion in Sect. 2.4 of Altwegg et al. (2017).
References. (1) Garrod (2013); (2) Belloche et al. (2013); (3) Neill et al. (2014); (4) Halfen et al. (2013); (5) Pagani et al. (2017), Laurent Pagani, priv. comm.; (6) Calcutt et al. (2018); (7) Ligterink et al. (2018); (8) Goesmann et al. (2015).

Although the variations in the column density of CH_3NH_2 over the studied regions are similar to those of CH_3OH and CH_3CN, the CH_3NH_2 excitation temperatures are higher than for any of the other species. This trend is most pronounced in the case of MM1. A relatively higher excitation temperature of CH_3NH_2 compared with other species is consistent with the findings of Halfen et al. (2013).

4.2. Methylamine towards other objects

Compared with the CH_3NH_2 to CH_3OH ratios derived by Belloche et al. (2013) and Neill et al. (2014) towards Sgr B2

(M) and (N), the values inferred for the regions in NGC 6334I are lower by up to two orders of magnitude, though the value derived for Sgr B2 (M) is only higher by a factor of three when compared with the value derived for MM1. For the CH_3NH_2 to NH_2CHO, CH_3CN, and CH_2NH ratios the picture is less clear; while the CH_3NH_2/NH_2CHO values derived towards Sgr B2 are all about an order of magnitude lower than those derived towards NGC 6334I, the CH_3NH_2/CH_3CN value derived by Neill et al. (2014) is higher by more than an order of magnitude while the values derived by Belloche et al. (2013) are lower by up to a factor of six. In the case of CH_3NH_2/CH_2NH, all but one of the values towards Sgr B2 are higher than the lower
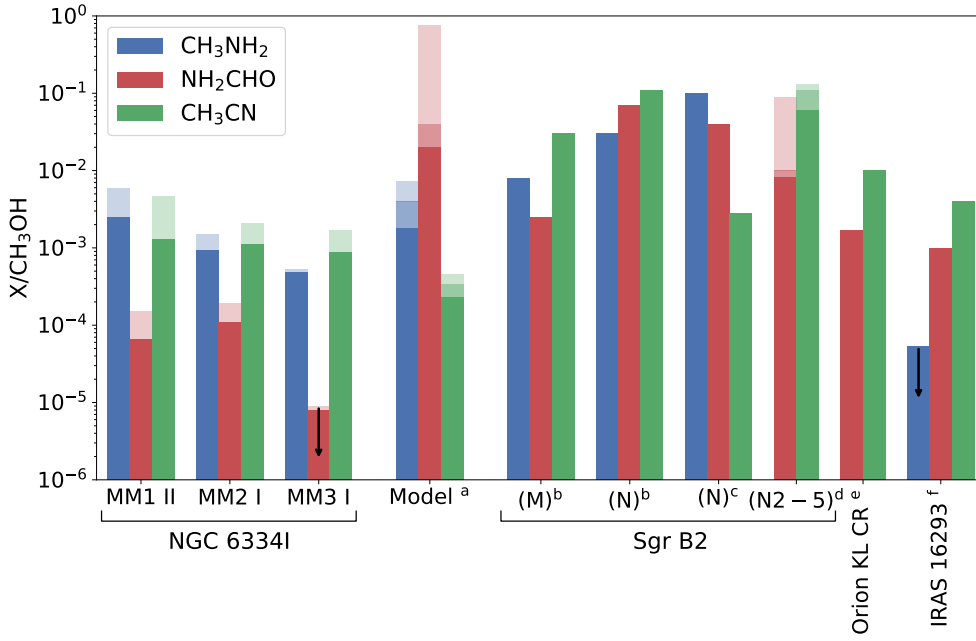
Fig. 3. Column density ratios of CH_3NH_2 (blue), NH_2CHO (red), and CH_3CN (green) with respect to CH_3OH for NGC 6334I, model predictions and other objects. For the regions in NGC 6334I, the shaded bars indicate the range of ratios derived using the ^{13}C- and ^{18}O-methanol isotopologues as base respectively. For the models, the shaded bars indicate the range of rations derived for the fast, medium and slow models respectively. For Sgr B2(N2–5), the shaded bars indicate the range of ratios derived for each of the components N2, N3, N4, and N5 (excluding the upper limit on NH_2CHO for N4). References. [a]Garrod (2013); [b]Belloche et al. (2013); [c]Neill et al. (2014); [d]Bonfand et al. (2017); [e]Crockett et al. (2014); [f]Ligterink et al. (2018).
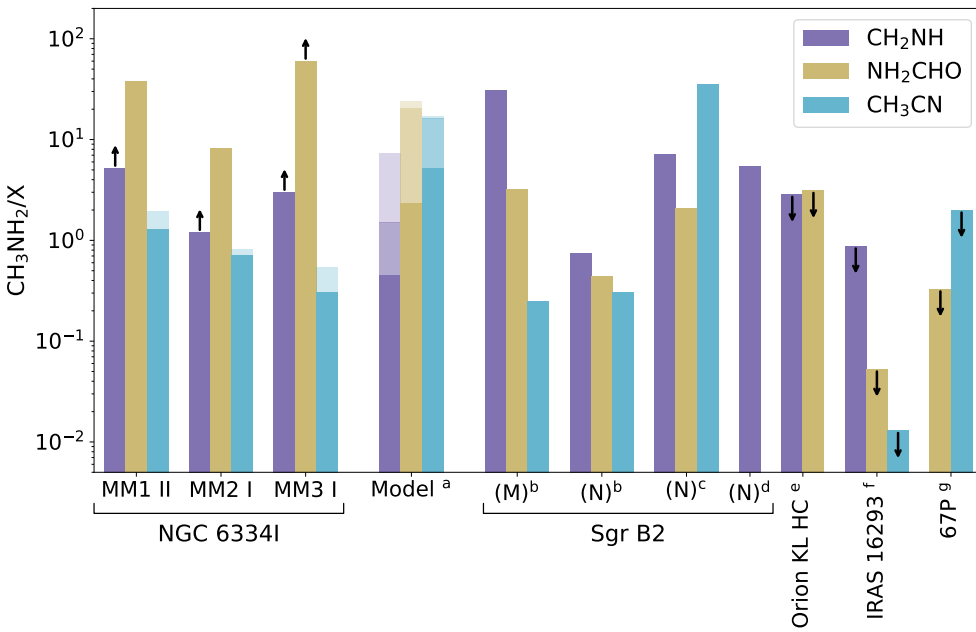

Fig. 4. Column density ratios of CH_3NH_2 with respect to CH_2NH (purple), NH_2CHO (gold), and CH_3CN (turquoise) for NGC 6334I, model predictions and other objects. For the regions in NGC 6334I, shaded bars indicate the range of ratios derived based on the $^{13}CH_3CN$ and $CH_3C^{15}N$ isotopologues. For the models, the shaded bars indicate the range of rations derived for the fast, medium and slow models respectively. References. [a]Garrod (2013); [b]Belloche et al. (2013); [c]Neill et al. (2014); [d]Halfen et al. (2013); [e]Pagani et al. (2017), Laurent Pagani, priv. comm.; [f]Ligterink et al. (2018); [g]Goesmann et al. (2015).

limits derived towards NGC 6334I. Because of these large variations it is difficult to make strong statements on the overall CH_3NH_2 distribution within the Sgr B2 region since chemical variations in the reference species are just as likely the source of the varying ratios. Also, due to the large distance to Sgr B2 (~8 kpc) and the fact that Belloche et al. (2013) and Neill et al. (2014) use single dish data, from the IRAM 30 m telescope and *Herschel* Space Observatory respectively, the observations may be biased towards large scale structures and particularly the effects of beam dilution should be considered since these studies probe spacial scales of the order of ~0.5–1 pc (~2×10^5 au) as compared with ~1300 au in the case of the regions in NGC 6334I.

In contrast to the studies of Sgr B2, the ALMA observations towards the Orion KL Hot Core region reported by Pagani et al. (2017) make for a more direct comparison with the observations towards NGC 6334I, since the Orion KL region is probed at

spacial scales of ~660 au. Though not firmly detected, the upper limits on the CH_3NH_2 to CH_2NH or NH_2CHO ratios hint that CH_3NH_2 is less abundant in the Orion KL hot core as compared with NGC 6334I or, alternatively, that NH_2CHO and CH_2NH are more abundant. Unfortunately the extended CH_3OH emission towards Orion KL could not be evaluated due to missing zero-spacing data. Without CH_3OH as a reference it is difficult to distinguish between the low-CH_3NH_2 and high-NH_2CHO or CH_2NH scenarios. In addition, the Orion KL data show that CH_3NH_2 is not associated with either NH_2CHO nor CH_2NH. This is based on the v_{LSR} which is 4.3 km s^{-1} for CH_3NH_2 but 5.5 km s^{-1} for NH_2CHO and CH_2NH. In NGC 6334I such a mismatch between velocity of different species is not observed toward either of the studied regions. Finally, as in the case of NGC 6334I, the excitation temperature is higher for CH_3NH_2 than for NH_2CHO and CH_2NH with values of 280, 200, and 150 K respectively.

The lowest CH_3NH_2 ratios are observed towards the low-mass protostar IRAS 16293–2422B, an analogue to the young Sun, where a deep upper limit on the column density of CH_3NH_2 was inferred by Ligterink et al. (2018), based on the ALMA PILS survey (see Jørgensen et al. 2016, for full PILS overview) probing spacial scales of ~60 au. This upper limit results in ratios with respect to CH_3OH, NH_2CHO, and CH_3CN which are all lower by one to two orders of magnitude when compared with the lowest ratios derived towards NGC 6334I. The smallest variation between NGC 6334I and IRAS 16293–2422B is seen in the CH_3NH_2 to CH_2NH ratio where the value derived for IRAS 16293–2422B is within the uncertainty of value derived for the MM2 I region but lower by up to a factor of six compared with the regions MM1 II and MM3 I. These differences in ratios hint that the formation of CH_3NH_2 in the high-mass hot cores of NGC 6334I differ from the formation of CH_3NH_2 in the low-mass IRAS 16293–2422B protostar. An explanation for this difference could be the dust grain temperature. Based on the low levels of CH_3OH deuteration in NGC 6334I, Bøgelund et al. (2018) determine a relatively warm dust grain temperature of ~30 K during the time of CH_3OH formation. In contrast, the dust grains in the cloud from which the IRAS 16293–2422 protobinary system formed are thought to have been much cooler, with temperatures below 20 K (Jørgensen et al. 2016). At high grain temperatures the solid-state formation of CH_3NH_2 via $CH_3 + NH_2$ could be enhanced, due to increased mobility of the radicals or the loss of H-atoms, which at lower temperatures would hydrogenate these radicals to form the neutral species CH_4 and NH_3.

Additional indications for a grain surface formation route are found in the chemical models presented by Garrod (2013). These models evaluate the chemical evolution of high-mass hot cores as these evolve through infall and warm-up phases. The physical model adopted by Garrod (2013) consists of a collapse phase followed by a gradual warm-up of the gas and dust. For the warm-up phase, three timescales are adopted: a "fast" scale reaching 200 K in 5×10^4 yr, a "medium" scale reaching 200 K in 2×10^5 yr, and a "slow" scale reaching 200 K in 1×10^6 yr. Listed in Tables 3 and 4 are the predicted peak gas-phase abundance ratios for each of these models. In the models, CH_3NH_2 is formed predominantly via CH_3 and NH_2 radical recombination reactions on the grain surface. Since the predicted CH_3NH_2 ratios are quite similar to the ratios derived for the regions in NGC 6334I, and for most species agree within a factor of five, a solid state formation pathway for CH_3NH_2 seems likely. However, since the models are not optimised to the physical conditions of the hot cores of NGC 6334 I but rather general conditions found in hot cores, the comparison between observed and modelled column density ratios should only be considered as indicative of trends.

4.3. Comparison with comet 67P

In an effort to understand how the life we know on Earth today has come to be, the chemical composition of the Solar Nebular must be examined. The most pristine record of this composition is believed to be locked up in comets. Goesmann et al. (2015) report the first in situ analysis of organic molecules on the surface of comet 67P. Based on the measurements of the COSAC instrument aboard Rosetta's Philae lander, Goesmann et al. (2015) derive CH_3NH_2 to NH_2CHO and CH_3CN ratios which are lower by one to two orders of magnitude for CH_3NH_2/NH_2CHO and higher by up to a factor of six for CH_3NH_2/CH_3CN, as compared with the values derived for NGC 6334I. To improve counting statistics, Goesmann et al. (2015) binned the COSAC

data in bins around integer mass numbers, thereby effectively reducing the mass resolution, before identifying and deriving abundances of the detected species. However, after reanalysing the unbinned COSAC data, and using higher resolution measurements from the ROSINA mass spectrometer, aboard the Rosetta orbiter, as a proxy for the near-surface cometary material, Altwegg et al. (2017) conclude that a revision of the list of molecules and derived abundances reported by Goesmann et al. (2015) is needed. Specifically, the contributions from CH_3NH_2, NH_2CHO, and CH_3CN to the signal in the COSAC data are likely to be significantly smaller than originally reported by Goesmann et al. (2015). Therefore, the CH_3NH_2 ratios for comet 67P are listed in this work as upper limits (following the discussion in Sect. 2.4 of Altwegg et al. 2017). The ratios derived for the comet are consistent with the values derived for the low-mass protostar IRAS 16293–2422B.

4.4. Other N-bearing species

For the NH_2CHO and CH_3CN to CH_3OH ratios, the variations derived for each of the NGC 6334I regions are small and within factors of between two and four (excluding the upper limit on NH_2CHO for region MM3 I which is about an order of magnitude lower than the values for MM1 II and MM2 I). Compared with the hot core model predictions of Garrod (2013), NH_2CHO/CH_3OH is over-predicted by orders of magnitude, while CH_3CN/CH_3OH, as is the case for CH_3NH_2/CH_3OH, shows fairly good agreement with the numbers derived for NGC 6334I.

For Sgr B2, the NH_2CHO and CH_3CN ratios with respect to CH_3OH show the same trends as CH_3NH_2/CH_3OH, and are generally one to two orders of magnitude higher than the values derived for NGC 6334I, though, as in the case of the CH_3NH_2 ratios, observations may suffer from beam dilution effects or underestimated CH_3OH values since only the main CH_3OH-isotope, which may be optically thick, is detected. Although CH_3NH_2 is not included in their study, the ratios derived for NH_2CHO and CH_3CN by Bonfand et al. (2017), using ALMA observations which probe scales of ~0.06 pc (~13300 au), indicate that the higher NH_2CHO and CH_3CN to CH_3OH ratios reported by Belloche et al. (2013) and Neill et al. (2014), are true and not artefacts of beam dilution or opacity effects. This implies that the chemical inventory of Sgr B2 is richer in complex nitrogen-bearing species than that of NGC 6334I, in agreement with the high temperatures and complexity characterising the Galactic central region. That the NGC 6334I region is relatively poor in N-bearing species is also in agreement with the findings of Suzuki et al. (2018) who investigate the correlation between O- and N-bearing species in a sample of eight hot cores and find that the former species are more abundant than the latter in this region.

For the Orion KL Compact Ridge, Crockett et al. (2014) use observations from *Herschel* to derive NH_2CHO/CH_3OH and CH_3CN/CH_3OH values which are generally lower than those derived for Sgr B2 but higher by at least an order of magnitude as compared with NGC 6334I.

Lastly, the ALMA observations towards the low-mass protostar IRAS 16293–2422B, indicate similar CH_3CN/CH_3OH values as compared with the regions in NGC 6334I, while the values for NH_2CHO/CH_3OH are higher for IRAS 16293–2422B by about an order of magnitude as compared with the values for the regions in NGC 6334I. The generally similar CH_3CN and NH_2CHO to CH_3OH ratios between NGC 6334I and IRAS 16293–2422B indicate that the overall lower CH_3NH_2 ratios derived towards IRAS 16293–2422B reflect an actual difference

in chemical composition between the two sources. As discussed above, this difference in CH$_3$NH$_2$ abundance may reflect a difference in grain temperature during the time when the species was formed. With the sensitivity and resolution provided by ALMA, continued studies of this and related species will broaden our understanding of the inventory of pre-biotic species in both high- and low-mass sources and help evaluate the degree to which CH$_3$NH$_2$ chemistry depends on the grain temperature.

5. Summary

In this work, we present the first detection of CH$_3$NH$_2$ towards NGC 6334I and derive the column density of the species in the hot cores MM1, MM2, and MM3. Transitions of CH$_2$NH, NH$_2$CHO, ^{13}CH$_3$CN, and CH$_3$C^{15}N are also studied and their column densities inferred. Assuming LTE and excitation temperatures in the range 70–340 K, each species is modelled separately and then summed to obtain a full spectrum for each of the studied regions. Based on the good agreement between the CH$_3$NH$_2$ column density ratios predicted by the hot core models of Garrod (2013) and the values derived for the regions in NGC 6334I, the formation of CH$_3$NH$_2$ is more likely to proceed via radical recombination reactions on grain surfaces than via gas-phase reactions.

The detection of CH$_3$NH$_2$ towards NGC 6334I reported here and recent (tentative) detections towards the high-mass starforming regions in Orion KL and G10.47+0.03 by Pagani et al. (2017) and Ohishi et al. (2017) respectively, also indicate that the species is not as uncommon in the ISM as was previously thought. This implies that future high-sensitivity, high-resolution searches for the species are likely to yield additional detections of the formerly so elusive molecule. In this case, observations carried out towards both high- and low-mass objects, will help assess the dependency of CH$_3$NH$_2$-grain formation efficiency on the dust grain temperature of individual regions.

References

Altwegg, K., Balsiger, H., Berthelier, J. J., et al. 2017, MNRAS, 469, S130
Aponte, J. C., Elsila, J. E., Glavin, D. P., et al. 2017, ACS Earth Space Chem., 1, 3
Belloche, A., Müller, H. S. P., Menten, K. M., Schilke, P., & Comito, C. 2013, A&A, 559, A47
Bisschop, S. E., Jørgensen, J. K., van Dishoeck, E. F., & de Wachter, E. B. M. 2007, A&A, 465, 913
Blanco, S., López, J. C., Lesarri, A., & Alonso, J. L. 2006, J. Am. Chem. Soc, 128, 12111
Bockelée-Morvan, D., Wink, J., Despois, D., et al. 1997, Earth Moon and Planets, 78, 67
Bøgelund, E. G., McGuire, B. A., Ligterink, N. F. W., et al. 2018, A&A, 615, A88
Bonfand, M., Belloche, A., Menten, K. M., Garrod, R. T., & Müller, H. S. P. 2017, A&A, 604, A60
Bossa, J.-B., Duvernay, F., Theulé, P., et al. 2009, A&A, 506, 601
Brogan, C. L., Hunter, T. R., Cyganowski, C. J., et al. 2016, ApJ, 832, 187
Calcutt, H., Jørgensen, J. K., Müller, H. S. P., et al. 2018, A&A, 616, A90
Cazaux, S., Tielens, A. G. G. M., Ceccarelli, C., et al. 2003, ApJ, 593, L51
Chibueze, J. O., Omodaka, T., Handa, T., et al. 2014, ApJ, 784, 114
Coutens, A., Jørgensen, J. K., van der Wiel, M. H. D., et al. 2016, A&A, 590, L6
Crockett, N. R., Bergin, E. A., Neill, J. L., et al. 2014, ApJ, 787, 112
Crovisier, J., Bockelée-Morvan, D., Colom, P., et al. 2004, A&A, 418, 1141
Danger, G., Borget, F., Chomat, M., et al. 2011, A&A, 535, A47
Dickens, J. E., Irvine, W. M., DeVries, C. H., & Ohishi, M. 1997, ApJ, 479, 307
Endres, C. P., Schlemmer, S., Schilke, P., Stutzki, J., & Müller, H. S. P. 2016, J. Mol. Spectr., 327, 95
Förstel, M., Bergantini, A., Maksyutenko, P., Góbi, S., & Kaiser, R. I. 2017, ApJ, 845, 83
Gardner, F. F., Godfrey, P. D., & Williams, D. R. 1980, MNRAS, 193, 713
Garrod, R. T. 2013, ApJ, 765, 60
Garrod, R. T., Widicus Weaver, S. L., & Herbst, E. 2008, ApJ, 682, 283
Goesmann, F., Rosenbauer, H., Bredehöft, J. H., et al. 2015, Science, 349, aab0689
Goldman, N., Reed, E. J., Fried, L. E., William Kuo, I.-F., & Maiti, A. 2010, Nat. Chem., 2, 949
Halfen, D. T., Ilyushin, V. V., & Ziurys, L. M. 2013, ApJ, 767, 66
Herbst, E., & van Dishoeck, E. F. 2009, ARA&A, 47, 427
Holtom, P. D., Bennett, C. J., Osamura, Y., Mason, N. J., & Kaiser, R. I. 2005, ApJ, 626, 940
Hunter, T. R., Brogan, C. L., MacLeod, G., et al. 2017, ApJ, 837, L29
Irvine, W. M., Dickens, J. E., Lovell, A. J., et al. 1998, Faraday Discuss., 109, 475
Jørgensen, J. K., van der Wiel, M. H. D., Coutens, A., et al. 2016, A&A, 595, A117
Jørgensen, J. K., Müller, H. S. P., Calcutt, H., et al. 2018, A&A, 620, A170
Kahane, C., Ceccarelli, C., Faure, A., & Caux, E. 2013, ApJ, 763, L38
Kaifu, N., Morimoto, M., Nagane, K., et al. 1974, ApJ, 191, L135
Kim, Y. S., & Kaiser, R. I. 2011, ApJ, 729, 68
Kirchhoff, W. H., Johnson, D. R., & Lovas, F. J. 1973, J. Phys. Chem. Ref. Data, 2, 1
Kukolich, S. G. & Nelson, A. C. 1971, Chem. Phys. Lett., 11, 383
Kumar, A., Sharma, R., & Kamaluddin. 2014, Astrobiology, 14, 769
Lee, C.-W., Kim, J.-K., Moon, E.-S., Minh, Y. C., & Kang, H. 2009, ApJ, 697, 428
Ligterink, N. F. W., Tenenbaum, E. D., & van Dishoeck, E. F. 2015, A&A, 576, A35
Ligterink, N. F. W., Calcutt, H., Coutens, A., et al. 2018, A&A, 619, A28
Matthews, C. N., & Minard, R. D. 2006, Faraday Discuss., 133, 393
McGuire, B. A., Shingledecker, C. N., Willis, E. R., et al. 2017, ApJ, 851, L46
McGuire, B. A., Brogan, C. L., Hunter, T. R., et al. 2018, ApJ, 863, L35
Milam, S. N., Savage, C., Brewster, M. A., Ziurys, L. M., & Wyckoff, S. 2005, ApJ, 634, 1126
Motiyenko, R. A., Tercero, B., Cernicharo, J., & Margulès, L. 2012, A&A, 548, A71
Motiyenko, R. A., Ilyushin, V. V., Drouin, B. J., Yu, S., & Margulès, L. 2014, A&A, 563, A137
Müller, H. S. P., Thorwirth, S., Roth, D. A., & Winnewisser, G. 2001, A&A, 370, L49
Müller, H. S. P., Schlöder, F., Stutzki, J., & Winnewisser, G. 2005, J. Mol. Struct., 742, 215
Müller, H. S. P., Drouin, B. J., & Pearson, J. C. 2009, A&A, 506, 1487
Mumma, M. J., & Charnley, S. B. 2011, ARA&A, 49, 471
Neill, J. L., Bergin, E. A., Lis, D. C., et al. 2014, ApJ, 789, 8
Öberg, K. I., Guzmán, V. V., Furuya, K., et al. 2015, Nature, 520, 198
Ohishi, M., Suzuki, T., Hirota, T., Saito, M., & Kaifu, N. 2017, PASJ, submitted [arXiv:1708.06871]
Pagani, L., Favre, C., Goldsmith, P. F., et al. 2017, A&A, 604, A32
Patel, B. H., Percivalle, C., Ritson, D. J., Duffy, C. D., & Sutherland, J. D. 2015, Nat. Chem., 7, 301
Persi, P., & Tapia, M. 2008, Star Formation in NGC 6334, ed. B. Reipurth, 456
Pickett, H. M., Poynter, R. L., Cohen, E. A., et al. 1998, J. Quant. Spectr. Rad. Transf., 60, 883
Reid, M. J., Menten, K. M., Brunthaler, A., et al. 2014, ApJ, 783, 130
Remijan, A. J., Milam, S. N., Womack, M., et al. 2008, ApJ, 689, 613
Saladino, R., Crestini, C., Ciciriello, F., Costanzo, G., & di Mauro, E. 2006, Orig. Life Evol. Biospheres, 36, 523
Saladino, R., Carota, E., Botta, G., et al. 2016, Orig. Life Evol. Biospheres, 46, 515
Suzuki, T., Ohishi, M., Hirota, T., et al. 2016, ApJ, 825, 79
Suzuki, T., Ohishi, M., Saito, M., et al. 2018, ApJS, 237, 3
Theule, P., Borget, F., Mispelaer, F., et al. 2011, A&A, 534, A64
Wilson, T. L. 1999, Rep. Prog. Phys., 62, 143
Woon, D. E. 2002, ApJ, 571, L177
Zernickel, A., Schilke, P., Schmiedeke, A., et al. 2012, A&A, 546, A87

Appendix A: Model grids

Table A.1. Overview of model grids.

Species	N_s range (cm^{-2})		
	MM1 II	MM2 I	MM3 I
CH$_2$NH	10^{16}–10^{17}	10^{16}–10^{17}	5×10^{14}–5×10^{15}
CH$_3$NH$_2$	5×10^{16}–5×10^{17}	3×10^{16}–3×10^{17}	10^{15}–10^{16}
^{13}CH$_3$CN	10^{15}–10^{16}	5×10^{14}–5×10^{15}	5×10^{13}–5×10^{14}
CH$_3$C^{15}N	10^{14}–10^{15}	10^{14}–10^{15}	5×10^{12}–5×10^{13}
NH$_2$CHO	5×10^{15}–5×10^{16}	5×10^{15}–5×10^{16}	10^{13}–10^{14}
NH$_2^{13}$CHO	5×10^{14}–5×10^{15}	10^{14}–10^{15}	–

Notes. All grids have T_{ex} spanning $10-500$ K in steps of 10 K and N_s sampled by 20 logarithmically spaced steps.

Appendix B: Integrated line intensities

This appendix lists the integrated intensities of the best-fit model for each species and region, along with the integrated intensity, FWHM and v_{LSR} of a gaussian profile fitted to selected line features in the observed spectra. However, due to the high line density in the observed spectra, the majority of the listed transitions are blended. Therefore, care should be taken when interpreting the integrated intensities of the observed transitions since these fits in the majority of cases cover blended features which cannot be disentangled and therefore will include the contributions from other (unknown) species.

Table B.1. Integrated intensities of spectral line features.

Transition		Region	I_{model} [b]	Fit to observed spectrum [a]		
				I_{gauss}	$FWHM_{gauss}$	$v_{LSR,gauss}$
(QN)$_{up}$ [c]	(QN)$_{low}$ [c]		(K km s^{-1})	(K km s^{-1})	(km s^{-1})	(km s^{-1})
			CH$_2$NH			
$15_{2,13}$ 14	$14_{3,12}$ 13	MM1*	46.2	37.8	2.7 ± 0.8	-8.2 ± 0.3
$15_{2,13}$ 16	$14_{3,12}$ 15	MM2*	36.8	24.1	2.4 ± 0.3	-10.4 ± 0.1
$15_{2,13}$ 15	$14_{3,12}$ 14	MM3	0.5	–	–	–
			CH$_3$NH$_2$ [d]			
16 2 A2 15	15 3 A1 14	MM1	18.3	–	–	–
16 2 A2 17	15 3 A1 16	MM2	4.8	–	–	–
16 2 A2 16	15 3 A1 16	MM3	0.2	–	–	–
13 2 B2 13	13 1 B1 13	MM1*	106.0	123.6	4.8 ± 0.8	-7.9 ± 0.2
13 2 B2 14	13 1 B1 14	MM2*	32.5	74.0	3.6 ± 0.3	-11.0 ± 0.1
13 2 B2 13	13 1 B1 12	MM3	1.7	2.0	3.2 ± 0.6	-10.9 ± 0.2
9 0 B2 8	8 1 B1 7	MM1	115.3	–	–	–
9 0 B2 10	8 1 B1 9	MM2	41.5	–	–	–
9 0 B2 9	8 1 B1 8	MM3*	2.2	2.4	4.4 ± 1.1	-10.7 ± 0.4
16 7 B1 16	17 6 B2 17					
16 7 B2 16	17 6 B1 17					
16 7 B1 17	17 6 B2 18	MM1	36.6	–	–	–
16 7 B2 17	17 6 B1 18	MM2	7.6	–	–	–
16 7 B1 15	17 6 B2 16	MM3	0.4	–	–	–
16 7 B2 15	17 6 B1 16					
9 0 E2+1 8	8 1 E2+1 7	MM1	38.8	–	–	–
9 0 E2+1 10	8 1 E2+1 9	MM2	13.7	–	–	–
9 0 E2+1 9	8 1 E2+1 8	MM3	0.7	–	–	–
			^{13}CH$_3$CN			
		MM1*	27.5	36.9	3.6 ± 0.6	-6.8 ± 0.3
17_5	16_5	MM2*	10.8	32.2	2.8 ± 0.2	-8.0 ± 0.1
		MM3	0.9	1.1	2.4 ± 0.3	-9.2 ± 0.1

Notes. [*]Fit to blended feature. [a]Gaussian fit to the observed line features. Listed values are the integrated intensity, FWHM and v_{LSR} of the fitted gaussian profile, including 1σ uncertainties. [b]Integrated intensity of the best-fit model for each region and spectral feature. [c]Quantum numbers for CH$_2$NH are $J_{Ka,Kc}$ F. Quantum numbers for CH$_3$NH$_2$ are J K_a Γ F, following the notation of Motiyenko et al. (2014). Quantum numbers for ^{13}CH$_3$CN and CH$_3$C^{15}N are J_K. Quantum numbers for NH$_2$CHO and NH$_2^{13}$CHO are $J_{Ka,Kc}$. [d]Only lines with $A_{ij} > 10^{-6}$ s^{-1} are listed.

Table B.1. continued.

Transition		Region	I_{model} [b]	Fit to observed spectrum [a]		
				I_{gauss}	$FWHM_{gauss}$	$v_{LSR,gauss}$
$(QN)_{up}$ [c]	$(QN)_{low}$ [c]		(K km s^{-1})	(K km s^{-1})	(km s^{-1})	(km s^{-1})
17_4	16_4	MM1*	49.0	38.1	2.6 ± 0.4	-6.5 ± 0.2
		MM2*	24.2	50.4	3.3 ± 0.3	-8.6 ± 0.1
		MM3	1.9	1.9	2.5 ± 0.2	-8.8 ± 0.1
17_3	16_3	MM1	132.1	108.1	3.5 ± 0.4	-6.4 ± 0.2
		MM2	80.9	86.2	3.4 ± 0.2	-8.3 ± 0.1
		MM3	6.7	7.1	2.3 ± 0.2	-8.7 ± 0.1
17_2	16_2	MM1*	100.4	124.5	4.4 ± 0.7	-6.7 ± 0.2
		MM2*	66.9	72.9	3.2 ± 0.2	-8.3 ± 0.1
		MM3*	5.1	5.2	2.4 ± 0.6	-8.6 ± 0.2
17_1	16_1	MM1*	113.1	212.7	4.3 ± 0.3	-7.5 ± 0.1
		MM2*	82.5	78.0	3.1 ± 0.3	-8.4 ± 0.1
		MM3*	6.6	7.5	2.3 ± 0.3	-8.7 ± 0.1
17_0	16_0	MM1	128.5	–	–	–
		MM2	91.8	–	–	–
		MM3	7.5	–	–	–
		CH$_3$C^{15}N				
17_4	16_4	MM1	8.3	–	–	–
		MM2	3.3	–	–	–
		MM3	0.3	–	–	–
17_1	16_1	MM1	26.0	23.7	2.5 ± 0.5	-6.3 ± 0.2
		MM2*	12.3	32.56	2.4 ± 0.2	-7.9 ± 0.1
		MM3	1.4	1.31	2.7 ± 0.6	-8.9 ± 0.2
17_2	16_2	MM1*	18.6	20.2	3.2 ± 0.5	-6.5 ± 0.2
		MM2*	9.8	23.0	3.8 ± 0.5	-7.7 ± 0.2
		MM3	1.2	0.65	1.6 ± 0.4	-8.5 ± 0.2
17_1	16_1	MM1	24.7	–	–	–
		MM2	13.0	–	–	–
		MM3	1.6	–	–	–
17_1	16_1	MM1	26.7	–	–	–
		MM2	16.5	–	–	–
		MM3	1.8	–	–	–
		NH$_2$CHO				
$15_{1,15}$	$14_{1,14}$	MM1	135.1	–	–	–
		MM2	172.0	–	–	–
		MM3	1.6	–	–	–
$14_{1,13}$	$13_{1,12}$	MM1	130.7	–	–	–
		MM2	168.3	–	–	–
		MM3	1.6	–	–	–
		NH$_2^{13}$CHO				
$15_{1,15}$	$14_{1,14}$	MM1	41.4	–	–	–
		MM2	13.2	–	–	–
		MM3	–	–	–	–
$14_{1,13}$	$13_{1,12}$	MM1	40.1	–	–	–
		MM2	12.9	–	–	–
		MM3	–	–	–	–

Appendix C: ALMA Band 10 spectrum of methylamine

The Band 10 spectrum was acquired as part of project ADS/JAO.ALMA#2017.1.00717.S. Because the primary beam at Band 10 is only ~7″, two pointing positions were needed to cover the entire source. Only one of those has been observed, the phase centre was α(J2000) = $17^h20^m53.3^s$ δ(J2000) = $-35°46'59''.0$. The spectrum presented in Fig. C.1 was extracted from a position with coordinates (J2000 $17^h20^m53.3^s$, $-35°46'59''.0$),

chosen off the bright continuum peak of MM1, to minimise the number of transitions driven into absorption. A detailed first look at the data is presented in McGuire et al. (2018). We present the spectrum here to support the identification of CH_3NH_2 in NGC 6334I, but caution that the excitation conditions and column density in these data at this position are not directly comparable to the Band 7 data discussed in this work. Table C.1 lists the catalogue frequencies and other spectroscopic data for the CH_3NH_2 transitions shown in Fig. C.1.
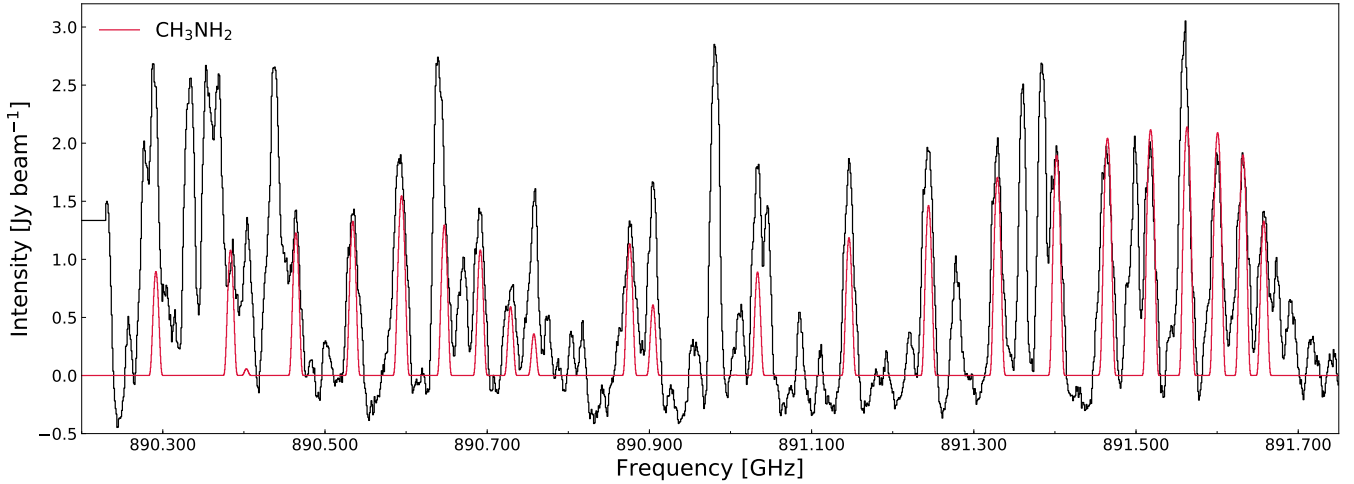

Fig. C.1. CH_3NH_2 transitions detected towards NGC 6334I in the range 890.2 to 891.7 GHz (ALMA Band 10). The red line represents the synthetic spectrum of CH_3NH_2 assuming a column density of 2×10^{17} cm^{-2}, an excitation temperature of 100 K and a FWHM line width of 3.2 km s^{-1}, in a $0''.26 \times 0''.26$ beam (equivalent to the angular resolution of the data). The abscissa is the rest frequency with respect to the radial velocity towards the region (-7 km s^{-1}). The data are shown in black.

Table C.1. Summary of the brightest CH_3NH_2 lines between 890.2 and 891.7 GHz.

Transition		Catalogue Frequency	E_{up}	A_{ij}	Catalogue
$(QN)_{up}$	$(QN)_{low}$	(MHz)	(K)	$\times 10^{-4}$ (s^{-1})	
13 6 E1-1 13	13 5 E1-1 13	890 291.6353	333.72	8.77	Motiyenko et al. (2014)
13 6 E1-1 14	13 5 E1-1 14	890 291.7865	333.72	9.61	
13 6 E1-1 12	13 5 E1-1 12	890 291.7981	333.72	8.18	
12 6 E1-1 12	12 5 E1-1 12	890 383.6647	306.08	8.57	
12 6 E1-1 13	12 5 E1-1 13	890 383.8427	306.08	9.39	
12 6 E1-1 11	12 5 E1-1 11	890 383.8576	306.08	8.00	
20 6 B2 20	20 5 B1 21	890 402.2366	589.75	9.80	
20 6 B2 21	20 5 B1 21	890 402.2883	586.75	10.3	
20 6 B2 19	20 5 B1 19	890 402.2909	586.75	9.33	
20 6 B1 20	20 5 B2 21	890 404.2829	589.75	9.80	
20 6 B1 21	20 5 B2 21	890 404.3348	586.75	10.3	
20 6 B1 19	20 5 B2 19	890 404.3374	586.75	9.33	
11 6 E1-1 11	11 5 E1-1 11	890 464.2275	280.56	8.18	
11 6 E1-1 12	11 5 E1-1 12	890 464.4391	280.56	8.97	
11 6 E1-1 10	11 5 E1-1 10	890 464.4584	280.56	7.64	
10 6 E1-1 10	10 5 E1-1 10	890 534.3699	257.17	7.64	
10 6 E1-1 11	10 5 E1-1 11	890 534.6247	257.17	8.57	
10 6 E1-1 9	10 5 E1-1 9	890 534.6502	257.17	6.96	
9 6 E1-1 9	9 5 E1-1 9	890 595.0509	235.9	6.96	
9 6 E1-1 10	9 5 E1-1 10	890 595.3625	235.9	7.81	
9 6 E1-1 8	9 5 E1-1 8	890 595.3973	235.9	6.35	

Notes. Quantum numbers are $J\ K_a\ \Gamma\ F$, following the notation of Motiyenko et al. (2014).

Table C.1. continued.

Transition		Catalogue Frequency	E_{up}	A_{ij}	Catalogue
$(QN)_{up}$	$(QN)_{low}$	(MHz)	(K)	$\times 10^{-4}$ (s^{-1})	
8 6 E1-1 8	8 5 E1-1 8	890 647.1409	216.76	6.07	
8 6 E1-1 9	8 5 E1-1 9	890 647.5298	216.76	6.96	
8 6 E1-1 7	8 5 E1-1 7	890 647.5788	216.76	5.41	
7 6 E1-1 7	7 5 E1-1 7	890 691.4204	199.74	4.82	
7 6 E1-1 8	7 5 E1-1 8	890 691.9184	199.74	5.53	
7 6 E1-1 6	7 5 E1-1 6	890 691.9903	199.74	4.20	
6 6 E1-1 6	6 5 E1-1 6	890 728.5759	184.85	2.90	
6 6 E1-1 7	6 5 E1-1 7	890 729.5759	184.85	3.49	
6 6 E1-1 5	6 5 E1-1 5	890 729.3469	184.85	2.53	
18 6 B2 18	18 5 B1 18	890 757.4027	503.88	9.61	
18 6 B2 19	18 5 B1 19	890 757.4734	503.88	10.3	
18 6 B1 18	18 5 B2 18	890 758.1200	503.88	9.61	
18 6 B1 19	18 5 B2 19	890 758.1908	503.88	10.3	
11 3 A1 11	10 2 A2 10	890 875.8080	175.87	7.94	
11 3 A1 12	10 2 A2 11	890 875.9815	175.87	8.71	
11 3 A1 10	10 2 A2 9	890 876.0048	175.87	7.24	
17 6 B1 17	17 5 B2 17	890 904.3890	465.64	9.61	
17 6 B1 18	17 5 B2 18	890 904.4711	465.64	10.3	
17 6 B1 16	17 5 B2 16	890 904.4759	465.64	8.97	
17 6 B2 17	17 5 B1 17	890 904.7947	465.64	9.61	
17 6 B2 18	17 5 B1 18	890 904.8768	465.64	10.1	
17 6 B2 16	17 5 B1 16	890 904.8816	465.64	8.97	
16 6 B2 16	16 5 B1 16	891 033.4246	429.50	9.39	
16 6 B2 17	16 5 B1 17	891 033.5198	429.50	10.1	
16 6 B2 15	16 5 B1 15	891 033.5258	429.50	8.97	
16 6 B1 16	16 5 B2 16	891 033.6460	429.50	9.39	
16 6 B1 17	16 5 B2 17	891 033.7412	429.50	10.1	
16 6 B1 15	16 5 B2 15	891 033.7472	429.50	8.97	
15 6 B1 15	15 5 B2 15	891 146.2027	395.48	9.18	
15 6 B1 16	15 5 B2 16	891 146.3132	395.48	9.84	
15 6 B2 15	15 5 B1 15	891 146.3187	395.48	9.18	
15 6 B1 14	15 5 B2 14	891 146.3206	395.48	8.77	
15 6 B2 16	15 5 B1 16	891 146.4292	395.48	9.84	
15 6 B2 14	15 5 B1 14	891 146.4366	395.48	8.77	
14 6 B2 14	14 5 B1 14	891 244.3081	363.58	9.18	
14 6 B1 14	14 5 B2 14	891 244.3661	363.58	9.18	
14 6 B2 15	14 5 B1 15	891 244.4368	363.58	9.84	
14 6 B2 13	14 5 B1 13	891 244.4460	363.58	8.57	
14 6 B1 15	14 5 B2 15	891 244.4948	363.58	9.84	
14 6 B1 13	14 5 B2 13	891 244.5040	363.58	8.57	
13 6 B1 13	13 5 B2 13	891 329.2209	333.82	8.77	
13 6 B2 13	13 5 B1 13	891 329.2483	333.82	8.77	
13 6 B1 14	13 5 B2 14	891 329.3714	333.82	9.61	
13 6 B1 12	13 5 B2 12	891 329.3831	333.82	8.18	
13 6 B2 14	13 5 B1 14	891 329.3989	333.82	9.61	
13 6 B2 12	13 5 B1 12	891 329.4106	333.82	8.18	
12 6 B2 12	12 5 B1 12	891 402.3183	306.18	8.57	
12 6 B1 12	12 5 B2 12	891 402.3306	306.18	8.57	
12 6 B2 13	12 5 B1 13	891 402.4958	306.18	9.39	
12 6 B1 13	12 5 B2 13	891 402.5081	306.18	9.39	
12 6 B2 11	12 5 B1 11	891 402.5107	306.18	8.00	
12 6 B1 11	12 5 B2 11	891 402.5229	306.18	8.00	
11 6 B1 11	11 5 B2 11	891 464.8770	280.66	8.18	
11 6 B2 11	11 5 B1 11	891 464.8820	280.66	8.18	
11 6 B1 12	11 5 B2 12	891 465.0882	280.66	8.97	
11 6 B2 12	11 5 B1 12	891 465.0932	280.66	8.97	
11 6 B1 10	11 5 B2 10	891 465.1075	280.66	7.46	
11 6 B2 10	11 5 B1 10	891 465.1125	280.66	7.46	

Table C.1. continued.

Transition		Catalogue Frequency	E_{up}	A_{ij}	Catalogue
$(QN)_{up}$	$(QN)_{low}$	(MHz)	(K)	$\times 10^{-4}$ (s^{-1})	
10 6 B2 10	10 5 B1 10	891 518.0731	257.26	7.64	
10 6 B1 10	10 5 B2 10	891 518.0750	257.26	7.64	
10 6 B2 11	10 5 B1 11	891 518.3275	257.26	8.57	
10 6 B1 11	10 5 B2 11	891 518.3294	257.26	8.57	
10 6 B2 9	10 5 B1 9	891 518.3531	257.26	6.96	
10 6 B1 9	10 5 B2 9	891 518.3550	257.26	6.96	
9 6 B1 9	9 5 B2 9	891 562.9831	235.99	6.96	
9 6 B2 9	9 5 B1 9	891 562.9838	235.99	6.96	
9 6 B1 10	9 5 B2 10	891 563.2945	235.99	7.81	
9 6 B2 10	9 5 B1 10	891 563.2952	235.99	7.81	
9 6 B1 8	9 5 B2 8	891 563.3294	235.99	6.35	
9 6 B2 8	9 5 B1 8	891 563.3300	235.99	6.35	
8 6 B2 8	8 5 B1 8	891 600.5836	216.85	6.07	
8 6 B1 8	8 5 B2 8	891 600.5838	216.85	6.07	
8 6 B2 9	8 5 B1 9	891 600.9724	216.85	6.96	
8 6 B1 9	8 5 B2 9	891 600.9725	216.85	6.96	
8 6 B2 7	8 5 B1 7	891 601.0213	216.85	5.41	
8 6 B1 7	8 5 B2 7	891 601.0215	216.85	5.41	
7 6 B1 7	7 5 B2 7	891 631.7493	199.83	4.82	
7 6 B2 7	7 5 B1 7	891 631.7493	199.83	4.82	
7 6 B1 8	7 5 B2 8	891 632.2472	199.83	5.66	
7 6 B2 8	7 5 B1 8	891 632.2473	199.83	5.66	
7 6 B1 6	7 5 B2 6	891 632.3190	199.83	4.29	
7 6 B2 6	7 5 B1 6	891 632.3191	199.83	4.29	
6 6 B1 6	6 5 B2 6	891 657.2500	184.94	2.97	
6 6 B2 6	6 5 B1 6	891 657.2500	184.94	2.97	
6 6 B1 7	6 5 B2 7	891 657.9096	184.94	3.49	
6 6 B2 7	6 5 B1 7	891 657.9096	184.94	3.49	
6 6 B1 5	6 5 B2 5	891 658.0209	184.94	2.53	
6 6 B2 5	6 5 B1 5	891 658.0209	184.94	2.53	

Appendix D: Methanimine, methyl cyanide and formamide

In this appendix, the detections of CH_2NH, the ^{13}C- and ^{15}N-methyl cyanide isotopologues, and NH_2CHO are discussed in detail. The detected lines and best-fit models are shown in Figs. D.1–D.3.

D.1. Methanimine CH_2NH

A single (hyperfine split) transition of CH_2NH is covered by the data. The CH_2NH transition, located at 302.565 GHz, and best-fit synthetic spectrum for each of the regions are included in Fig. D.3. Unfortunately, the CH_2NH feature is situated in the wing of a much stronger transition, located at approximately 302.562 GHz, identified as CH_3OCHO. It should be noted however, that the peak in the data at 302.562 GHz is only partly reproduced by the synthetic spectrum of CH_3OCHO and additional contributions to the peak from other species, which are not included in the JPL or CDMS molecular databases, can therefore not be excluded. Because of this blend, we report only upper limits on the column density of CH_2NH in each of the studied regions. The CH_2NH column densities are $\leq 5.2 \times 10^{16}$ cm^{-2} assuming $T_{ex} = 215$ K for MM1 II, $\leq 5.0 \times 10^{16}$ cm^{-2} assuming $T_{ex} = 165$ K for MM2 I, and $\leq 10^{15}$ cm^{-2} assuming $T_{ex} = 120$ K for MM3 I.

D.2. Methyl cyanide CH_3CN

There are no transitions of the main CH_3CN isotopologue covered by the observations but six transitions belonging to the ^{13}C- and five transitions belonging to the ^{15}N-methyl cyanide isotopologues are within the data range. Based on these, the column density of the main CH_3CN isotopologue is derived assuming a ^{12}C/^{13}C value of 62 and a ^{14}N/^{15}N value of 422, both derived assuming $d_{GC} = 7.02$ kpc and the ^{12}C/^{13}C and ^{14}N/^{15}N relations presented by Milam et al. (2005) and Wilson (1999), respectively. The detected transitions of both ^{13}CH$_3$CN and CH$_3$C^{15}N belong to the $J = 17 \rightarrow 16$ series around 303.6 and 303.2 GHz, respectively, and have upper state energies in the range 131 to 310 K. No transitions of the ^{13}C-methyl cyanide isomer CH$_3^{13}$CN are covered by the data. Figures D.1 and D.2 show the detected methyl cyanide transitions and best-fit models.

MM1 II. In the case of MM1 II, the best-fit methyl cyanide column densities and excitation temperature are 3.4×10^{15} cm^{-2} and 70 K for ^{13}CH$_3$CN, respectively, and 3.3×10^{14} cm^{-2} and 110 K for CH$_3$C^{15}N, respectively. For ^{13}CH$_3$CN, the uncertainty on N_s and T_{ex} is approximately 30 and 15%, respectively, while for CH$_3$C^{15}N, the approximate uncertainty is 15 and 45%, respectively. The ratio of the column densities of ^{13}CH$_3$CN to CH$_3$C^{15}N is a factor of 10, higher than the expected value

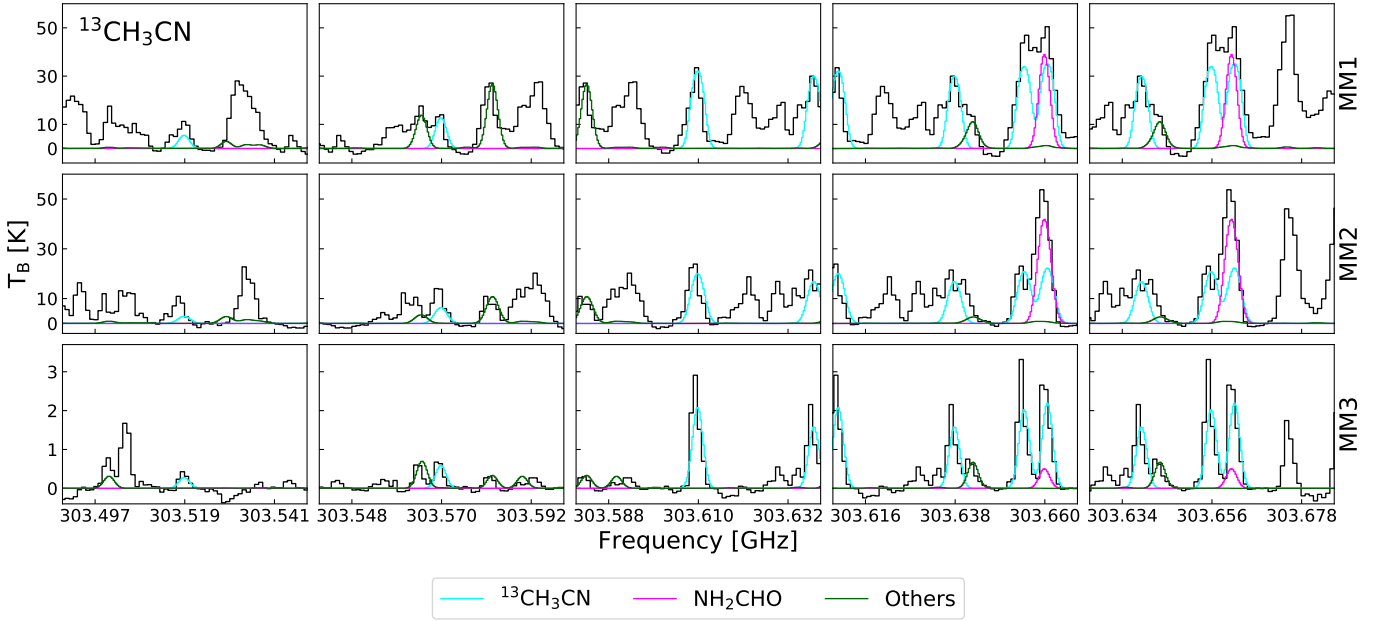**Fig. D.1.** $^{13}CH_3CN$ transitions detected towards NGC 6334I. Turquoise, magenta and green lines represent the synthetic spectrum of $^{13}CH_3CN$ and NH_2CHO and the sum of spectra of other contributing species respectively. The abscissa is the rest frequency with respect to the radial velocity towards each of the hot cores (listed in Table 2). The data are shown in black. *Top panels*: MM1 II. *Middle panels*: MM2 I. *Bottom panels*: MM3 I.
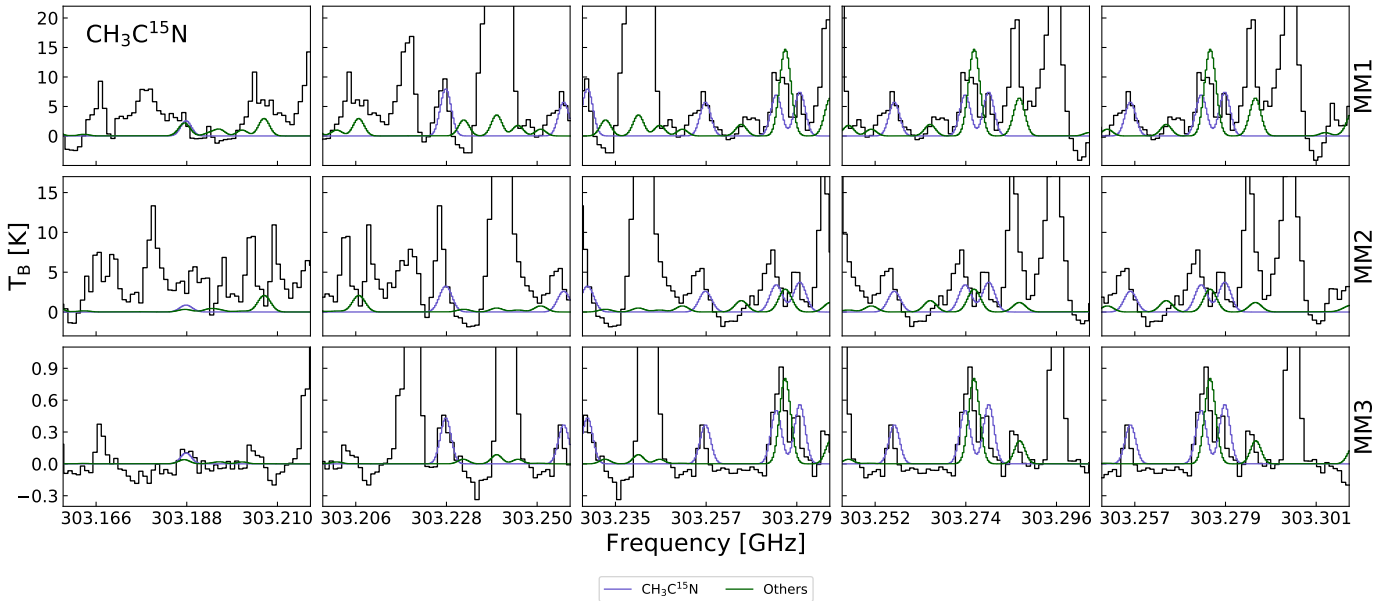

Fig. D.2. $CH_3C^{15}N$ transitions detected towards NGC 6334I. Blue and green lines represent the synthetic spectrum of $CH_3C^{15}N$ and the sum of spectra of other contributing species respectively. The abscissa is the rest frequency with respect to the radial velocity towards each of the hot cores (listed in Table 2). The data are shown in black. *Top panels*: MM1 II. *Middle panels*: MM2 I. *Bottom panels*: MM3 I.

of 6.8 based on the $^{12}C/^{13}C$ and $^{14}N/^{15}N$ relations. Of the six detected transitions belonging to $^{13}CH_3CN$, five are largely uncontaminated by emission from other species and can be assigned distinct peaks in the data. The final transition, located at 303.661 GHz, is blended with a transition of NH_2CHO (to be discussed in detail below). The sum of the best-fit spectra of $^{13}CH_3CN$ and NH_2CHO results in a model with a peak that is ~45% more intense than the data at 303.661 GHz. Optimising the column density of the $^{13}CH_3CN$ model to fit the blended transition results in underestimated model peak intensities for the remaining $^{13}CH_3CN$ lines with respect to the data.

The best-fit column density optimised to the blended line is a factor two lower than the best-fit column density when optimising to all $^{13}CH_3CN$ transitions. In contrast to $^{13}CH_3CN$, the transitions of $CH_3C^{15}N$ are mostly blended and only two of the five transitions, located at 303.228 and 303.257 GHz, can be assigned distinct counterparts in the data. The remaining transitions are blended with transitions of CH_3SH located around 303.187 and 303.276 GHz respectively. Excluding the contribution from CH_3SH to the model does not change the value of the best-fit column density of $CH_3C^{15}N$ but it should be noted that the summed best-fit spectra of $CH_3C^{15}N$ and

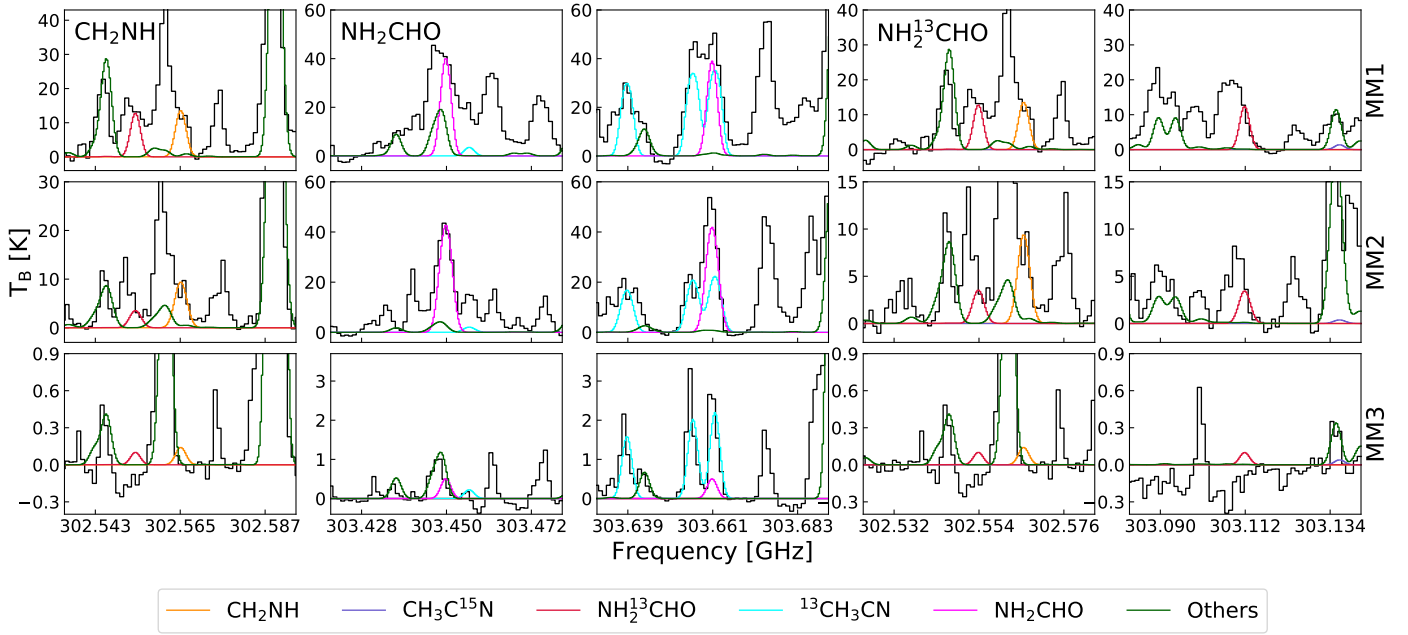**Fig. D.3.** CH_2NH, NH_2CHO and $NH_2^{13}CHO$ transitions detected towards NGC 6334I. Orange, magenta, red and green lines represent the synthetic spectrum of CH_2NH, NH_2CHO and $NH_2^{13}CHO$ and the sum of spectra of other contributing species respectively. The abscissa is the rest frequency with respect to the radial velocity towards each of the hot cores (listed in Table 2). The data are shown in black. *Top panels*: MM1 II. *Middle panels*: MM2 I. *Bottom panels*: MM3 I.

CH_3SH overshoot the data feature located at 303.276 GHz with approximately 50%.

MM2 I. The best-fit excitation temperature and column density for $^{13}CH_3CN$ in the MM2 I region is 80 K and 1.4×10^{15} cm^{-2}, respectively. For $CH_3C^{15}N$, the excitation temperature is not well contained and therefore the best-fit excitation temperature for $^{13}CH_3CN$ is adopted. For this temperature, the best-fit column density is 1.8×10^{14} cm^{-2}. The uncertainty on N_s and T_{ex} is approximately 30% in the case of $^{13}CH_3CN$ and 20% in the case of $CH_3C^{15}N$. As is the case of MM1 II, a single $^{13}CH_3CN$ line and three $CH_3C^{15}N$ lines are contaminated by emission from NH_2CHO and CH_3SH respectively. However, while the best-fit $^{13}CH_3CN$ column density optimised purely based on the unblended transitions is higher by ~20% with respect to the value derived when all transitions are included, the best-fit column density of $CH_3C^{15}N$ remains the same. The sum of spectra of $^{13}CH_3CN$ and NH_2CHO results in a model peak which is 15% brighter than the data at the location of the blended $^{13}CH_3CN$ line while including the contribution from CH_3SH to the model of $CH_3C^{15}N$ has only little effect on the summed spectra. The $^{13}CH_3CN$ to $CH_3C^{15}N$ ratio is lower than the ratio derived for MM1 II and has a value of 7.8.

MM3 I. The best-fit methyl cyanide column densities in region MM3 I are lower than for both MM1 II and MM2 I with values of 9×10^{13} cm^{-2} for $^{13}CH_3CN$ and 2.3×10^{13} cm^{-2} for $CH_3C^{15}N$, with excitation temperatures of 90 and 70 K, respectively. The uncertainty on N_s and T_{ex} is approximately 10 and 20%, respectively, for $^{13}CH_3CN$ and 30% and a factor of two, respectively, for $CH_3C^{15}N$. The ratio of the $^{13}CH_3CN$ to $CH_3C^{15}N$ column density is a factor of 3.9, lower than the expected value. For $^{13}CH_3CN$ as well as for $CH_3C^{15}N$, the best-fit column density remains unchanged when contributions from blending species are included in the synthetic spectrum.

D.3. Formamide NH_2CHO

While a total of 18 NH_2CHO transitions are covered by the data, only two are bright enough to be detected towards the NGC 6334I region. As discussed above, one of these lines, located at 303.661 GHz, is blended with a transition of $^{13}CH_3CN$. The second transition, located at 303.450 GHz, is also blended but with emission from CH_3SH. Figure D.3 shows the transitions and the best-fit model for each of the regions. In addition to the main NH_2CHO isotopologue, two transitions of $NH_2^{13}CHO$ are within the data range. Transitions belonging to the ^{15}N- and deuterated formamide isotopologues are too weak to be detected.

MM1 II. The synthetic spectrum that best reproduces the NH_2CHO lines detected towards the MM1 II region has a column density of 7.0×10^{15} cm^{-2}, assuming an excitation temperature of 215 K. The uncertainty on N_s is approximately 25%. In Sect. D.2 the NH_2CHO line blended with $^{13}CH_3CN$ was discussed and it was concluded that the sum of the optimised $^{13}CH_3CN$ and NH_2CHO spectra results in a modelled spectrum which overshoots the data by approximately 45%. The second detected NH_2CHO transition is blended with CH_3SH. However, the contribution from this species to the data feature at the location of the NH_2CHO transition is small. Excluding the contribution from CH_3SH to the full spectrum, results in a best-fit NH_2CHO column density which is less than a factor of two higher than the best-fit value which includes the blending species. For $NH_2^{13}CHO$ the best-fit column density is $\leq 2.0 \times 10^{15}$ cm^{-2} assuming an excitation temperature of 215 K. Both the detected transitions of $NH_2^{13}CHO$ are located in the wing of brighter emission lines and therefore, as in the case of CH_2NH, the best-fit model parameters are listed as upper limits only. Neither of the features blended with the $NH_2^{13}CHO$ transitions are reproduced by the modelled spectra of the potential blending species listed in Table E.1.

MM2 I. For region MM2 I the best-fit column densities are 7.6×10^{15} cm^{-2} and $\leq 5.0 \times 10^{14}$ cm^{-2} for NH$_2$CHO and NH$_2^{13}$CHO respectively, both assuming an excitation temperature of 165 K. The uncertainty on the column density of NH$_2$CHO is ~10%. As in the case of MM1 II, both the blended NH$_2$CHO transitions are slightly overproduced with respect to the data when the modelled spectra of ^{13}CH$_3$CN and other blending species are included in the fit. Excluding these blending species however, only increases the best-fit NH$_2$CHO column density by 10%. As in the case of MM1 II, the NH$_2^{13}$CHO column density is listed as an upper limit.

MM3 I. In region MM3 I only the transitions of the main NH$_2$CHO isotopologue are detected. However, since the data features at the locations of the NH$_2$CHO transitions can also

be reproduced by the respective blending species ^{13}CH$_3$CN and CH$_3$SH, the detection of NH$_2$CHO in this region is tentative and its column density reported as an upper limit. The best-fit modelled spectrum of NH$_2$CHO has a column density of $\leq 5.0 \times 10^{13}$ cm^{-2} assumes an excitation temperature of 120 K.

Appendix E: Potential blending species

In this appendix, a list of the potential blending species and the column densities and excitation temperatures used to fit them, is presented. The species have transitions which overlap in frequency with transitions of CH$_3$NH$_2$, CH$_2$NH, NH$_2$CHO, or the CH$_3$CN isotopologues and may therefore be contributing to the observed spectrum extracted from each of the studied regions.

Table E.1. Model parameters of potential blending species.

Species	Catalogue	MM1 II		MM2 I		MM3 I	
		N_s (cm^{-2})	T_{ex} (K)	N_s (cm^{-2})	T_{ex} (K)	N_s (cm^{-2})	T_{ex} (K)
^{13}CH$_3$OH[a]	CDMS	7.4×10^{17}	[215]	6.6×10^{17}	[165]	9.0×10^{16}	[120]
CH$_3^{18}$OH[a]	CDMS	2.0×10^{17}	[215]	8.0×10^{16}	[165]	1.4×10^{16}	[120]
C$_2$H$_5$OH	JPL	5.0×10^{17}	[215]	2.0×10^{17}	[300]	6.0×10^{15}	[200]
CH$_3$CH$_2$OD	CDMS	5.0×10^{15}	[215]	6.0×10^{15}	[165]	6.0×10^{14}	[50]
CH$_2$DCH$_2$OH	CDMS	5.0×10^{15}	[215]	3.0×10^{15}	[165]	2.0×10^{14}	[50]
CH$_3$SH	CDMS	3.0×10^{16}	[215]	$<1.0 \times 10^{16}$	[165]	1.0×10^{15}	[120]
C$_2$H$_3$CN	CDMS	1.0×10^{15}	[215]	$<1.0 \times 10^{15}$	[165]	–	–
^{13}CH$_2$CHCN	CDMS	8.0×10^{14}	[215]	2.0×10^{14}	[165]	–	–
CH$_3$COCH$_3$	JPL	1.5×10^{17}	[215]	2.0×10^{17}	[165]	2.0×10^{15}	[120]
CH$_3$OCHO	JPL	1.2×10^{17}	[215]	2.5×10^{17}	[165]	9.0×10^{16}	[120]
HCOCH$_2$OH	JPL	3.5×10^{16}	[215]	8.0×10^{15}	[165]	–	–
C$_2$H$_5$SH	CDMS	3.0×10^{16}	[215]	4.0×10^{16}	[165]	7.0×10^{14}	[120]
CH$_3$C$_3$N	CDMS	1.0×10^{15}	[215]	5.0×10^{14}	[165]	5.0×10^{13}	[120]
C$_3$H$_7$CN	CDMS	5.0×10^{15}	[215]	5.0×10^{15}	[165]	–	–

Notes. All models assume $\theta_s = 1''0$, $v_{LSR} = -6.7$ km s^{-1} for MM1 II and $v_{LSR} = -9.0$ km s^{-1} for MM2 I and MM3 I, and *FWHM* = 3.5 km s^{-1} for MM2 I and *FWHM* = 3.0 km s^{-1} for MM1 II and MM3 I. N_s is the highest value consistent with the data. [a]Values from Bøgelund et al. (2018).